



Personalized Predictions of Glioblastoma Infiltration: Mathematical Models, Physics-Informed Neural Networks and Multimodal Scans

Ray Zirui Zhang^{a,*}, Ivan Ezhov^b, Michał Balcerak^d, Andy Zhu^c, Benedikt Wiestler^b, Bjoern Menze^d, John S. Lowengrub^{a,e,*}

^aDepartment of Mathematics, University of California Irvine, USA

^bTechnical University of Munich, Germany

^cCarnegie Mellon University, USA

^dUniversity of Zurich, Switzerland

^eDepartment of Biomedical Engineering, University of California Irvine, USA

arXiv:2311.16536v3 [cs.LG] 16 Aug 2024

ARTICLE INFO

Article history:

Keywords: Inverse modeling, Physics-Informed Neural Networks, Glioma, Model calibration, MRI, radiotherapy

ABSTRACT

Predicting the infiltration of Glioblastoma (GBM) from medical MRI scans is crucial for understanding tumor growth dynamics and designing personalized radiotherapy treatment plans. Mathematical models of GBM growth can complement the data in the prediction of spatial distributions of tumor cells. However, this requires estimating patient-specific parameters of the model from clinical data, which is a challenging inverse problem due to limited temporal data and the limited time between imaging and diagnosis. This work proposes a method that uses Physics-Informed Neural Networks (PINNs) to estimate patient-specific parameters of a reaction-diffusion partial differential equation (PDE) model of GBM growth from a single 3D structural MRI snapshot. PINNs embed both the data and the PDE into a loss function, thus integrating theory and data. Key innovations include the identification and estimation of characteristic non-dimensional parameters, a pre-training step that utilizes the non-dimensional parameters and a fine-tuning step to determine the patient specific parameters. Additionally, the diffuse domain method is employed to handle the complex brain geometry within the PINN framework. The method is validated both on synthetic and patient datasets, and shows promise for real-time parametric inference in the clinical setting for personalized GBM treatment.

© 2024 Elsevier B. V. All rights reserved.

1. Introduction

Glioblastoma (GBM) is a common and very aggressive form of brain tumor, with a median survival of 15 months (Stupp et al., 2014, 2005). The current standard of care for GBM includes immediate resection of the visible tumor after diagnosis, followed by radiotherapy and chemotherapy targeting residual

tumor (Fernandes et al., 2017). Despite intensive treatment, the prognosis of GBM remains poor, as almost all GBMs recur. The high recurrence rate of GBM is attributed to its infiltrative nature. Instead of forming a clear boundary, the tumor invades into the surrounding normal-looking brain tissue (Souhami et al., 2004; Halperin et al., 1989) The infiltration pattern of tumor cells is heterogeneous and varies significantly among patients. Consequently, the standard clinical target vol-

*Corresponding authors: zirui.zhang@uci.edu, jlowengr@uci.edu

ume (CTV) of radiotherapy, which extends 1.5-3 cm uniformly from the visible tumor, may be insufficient for optimal coverage and distribution (Stupp et al., 2005). A critical step towards enhancing radiotherapy treatment planning requires the estimation of tumor cell distributions in a data-driven and patient-specific manner (Lipková et al., 2019; Unkelbach et al., 2014; Rockne et al., 2010, 2015, 2019).

Mathematical models of tumor growth are instrumental in predicting tumor progression and guiding individualized treatment decisions for patients (Baldock et al., 2013; Lipková et al., 2019; Butner et al., 2022; Ezhov et al., 2023; Chaudhuri et al., 2023; Subramanian et al., 2023; Lorenzo et al., 2023; Wu et al., 2022). The growth of GBM is often modeled using partial differential equations (PDEs) of reaction-diffusion type, which describe the spatio-temporal evolution of tumor cell density and captures the main tumor behavior: proliferation and infiltration (Harpold et al., 2007). More advanced models incorporate additional features including the mass effect (Hogea et al., 2007; Subramanian et al., 2019; Lipková et al., 2022), angiogenesis (Macklin et al., 2009; Saut et al., 2014; Yan et al., 2017), chemotaxis (Lu et al., 2022, 2023), and multiple species (Curtin et al., 2020; Yan et al., 2017). For comprehensive reviews on mathematical modeling of GBM, see Alfonso et al. (2017); Falco et al. (2021); Jørgensen et al. (2023).

To apply these models in a clinical setting, it is imperative to estimate patient-specific parameters of the PDEs from clinical data, which is a challenging inverse problem. Besides being useful in solving the PDE to predict tumor cell density profiles, these patient-specific parameters are valuable on their own as biophysics-based features to improve patient stratification and survival prediction. For example, recent studies show that these biophysical features correlate better with survival time than volumetric features from images (Subramanian et al., 2023). Further, the ratio of proliferation rate to diffusion rate is key in evaluating the effectiveness of supramarginal resection for IDH-wildtype GBM patients (Tripathi et al., 2021).

The inverse problem is commonly solved in the framework of PDE constrained optimization (Mang et al., 2012; Hogea

et al., 2008; Scheufele et al., 2020, 2021; Subramanian et al., 2020b,a, 2023) or Bayesian inference (Menze et al., 2011; Lipková et al., 2019; Ezhov et al., 2019, 2022a). Machine learning approaches have also been explored to speed up the computations, including learning surrogate models for forward PDE systems (Ezhov et al., 2022a), learning mappings from observations to parameters directly (Pati et al., 2021; Ezhov et al., 2023; Martens et al., 2022), using dynamic mode decomposition to construct low-dimensional representations (Viguerie et al., 2022), and optimizing discrete loss frameworks that integrate the PDE and the data using mesh-based discretizations (Karnakov et al., 2022; Balcerak et al., 2023). Instead of the full reaction-diffusion model, its asymptotic properties can be exploited to obtain an approximate anisotropic Eikonal approximation, which simplifies parameter estimation and tumor cell density prediction, albeit with a less detailed model (Konukoglu et al., 2010a,b; Unkelbach et al., 2014).

Physics-Informed Neural Networks (PINNs) have emerged as a novel method for solving inverse problems in a PDE constrained optimization framework (Karniadakis et al., 2021; Raissi et al., 2019; Jagtap et al., 2022a,b; Chen et al., 2020; Zheng et al., 2023; Huang et al., 2022). In this approach, PINNs represent the PDE solution as a neural network and embed both the data and the PDE, via a mesh-free approach using automatic differentiation, into the loss function. By minimizing the total loss, PINNs effectively solve the PDE and fit the data simultaneously, showcasing integration of mathematical models with data-driven learning processes. This is particularly beneficial in the realm of medical image analysis, where clinical measurements are often sparse and expensive. PINNs have been employed to combine the transcranial doppler data of blood flow velocity measurements and PDEs that govern the flow rate, pressure, and vessel area to estimate the brain hemodynamics (Sarabian et al., 2022). PINNs have also been used to calibrate the parameters in tracer-kinetic models with perfusion MR data for quantification of myocardial blood flow (van Herten et al., 2022). The potential for solving GBM inverse problems with PINNs was explored in Zhu (2022) using synthetic cell density

data.

In this work, we make personalized predictions of GBM tumor cell density distributions beyond the mass visible in medical scans by using solutions of a reaction-diffusion PDE model with parameters estimated from 3D structural MRI snapshots at a single time point. Fig. 1 provides an overview of our approach. Our data comprises a single snapshot of T1 gadolinium enhanced (T1Gd) and fluid attenuation inversion recovery (FLAIR) MRI scans. We combine the PDE model with an image model that relates the segmentation with the tumor cell density through thresholding. We overcome the challenge of inferring parameters using single time point data by identifying time-independent parameters, appropriately non-dimensionalizing the model and inferring the non-dimensional parameters. We use PINNs to solve the PDE and estimate the parameters from the data. The estimated parameters are used to predict tumor cell densities and aid personalized radiotherapy treatment planning. We validate our approach on synthetic data and patient data, where we can compute quantitative metrics such as DICE score of the segmentation, and compare the predicted infiltration pattern with observed tumor recurrence.

Our contributions are as follows: (1) We show that PINN is an effective and efficient method for solving the inverse problem of PDE parameter estimation in GBM using structural MRI data at a single time point, which is the most common clinical data available. (2) A simple procedure is introduced to estimate patient-specific non-dimensional characteristic parameters, which aid in scaling the PDE to address the single-time inference limitation. (3) We propose an effective two-step training procedure: in the pre-training step, we leverage the patient-specific non-dimensional characteristic parameters to train the PINN to learn the characteristic solution of the PDE. This serves as an excellent starting point for the fine-tuning stage, where we train the PINN to learn patient-specific parameters. (4) We introduce the diffuse domain method to handle the complex brain geometry in the PINN framework.

In the remainder of the paper, Section 2 elucidates the components of our methods, including the mathematical model of

tumor growth (Section 2.1), the workflow of the parameter estimation process (Section 2.2), and the loss functions used for training the PINN (Section 2.3). The results are presented in Section 3, where we first validate our approach on synthetic data (Section 3.1), and then apply our approach to patient data (Section 3.2). In Section 3.3, we also discuss the merits and limitations of our approach, compared with other methods. Conclusions are presented in Section 4. Additional technical details and results are given in the appendices.

2. Methods

2.1. Model

2.1.1. Tumor Model

We consider the Fisher-KPP PDE, a fundamental model that describes the spatio-temporal evolution of the normalized tumor cell density $u(\mathbf{x}, t)$ in a 3D domain Ω consisting of white matter (WM) and grey matter (GM) regions (Harpold et al., 2007; Swanson et al., 2000). The PDE, with Neumann boundary conditions, is given by

$$\begin{cases} \frac{\partial u}{\partial t} = \nabla \cdot (\mathbb{D}(\mathbf{x}) \nabla u) + \rho u(1 - u) & \text{in } \Omega \\ \nabla u \cdot \mathbf{n} = 0 & \text{on } \partial\Omega \end{cases} \quad (1)$$

where ρ [1/day] is the proliferation rate and $\mathbb{D}(\mathbf{x})$ [mm²/day] is the diffusion tensor, and \mathbf{n} is the outward normal vector on the boundary $\partial\Omega$. We further assume that the diffusion is isotropic, and is a weighted sum of the diffusion coefficient in WM and GM, $\mathbb{D}(\mathbf{x}) = D_w P_w(\mathbf{x}) + D_g P_g(\mathbf{x})$, where P_w, P_g are the percentages of white and grey matter, and D_w, D_g [mm²/day] are the diffusion coefficient in white and grey matter, and $D_w = 10D_g$ (Menze et al., 2011; Lipková et al., 2019; Swanson et al., 2000). Therefore, the original PDE (1) can be written as

$$\frac{\partial u}{\partial t} = D \nabla \cdot (P(\mathbf{x}) \nabla u) + \rho u(1 - u) \quad \text{in } \Omega \quad (2)$$

where $D = D_w$ is the scalar diffusion coefficient in white matter, and $P(\mathbf{x}) = P_w(\mathbf{x}) + 10P_g(\mathbf{x})$ defines the geometry of the brain. We use an atlas-guided approach to obtain the brain geometry and tissue percentages. In particular, we register the brain atlas used in Lipková et al. (2019) to patient T1w scans using rigid registration following Lipková et al. (2019). While rigid registration works well in many cases, some errors may

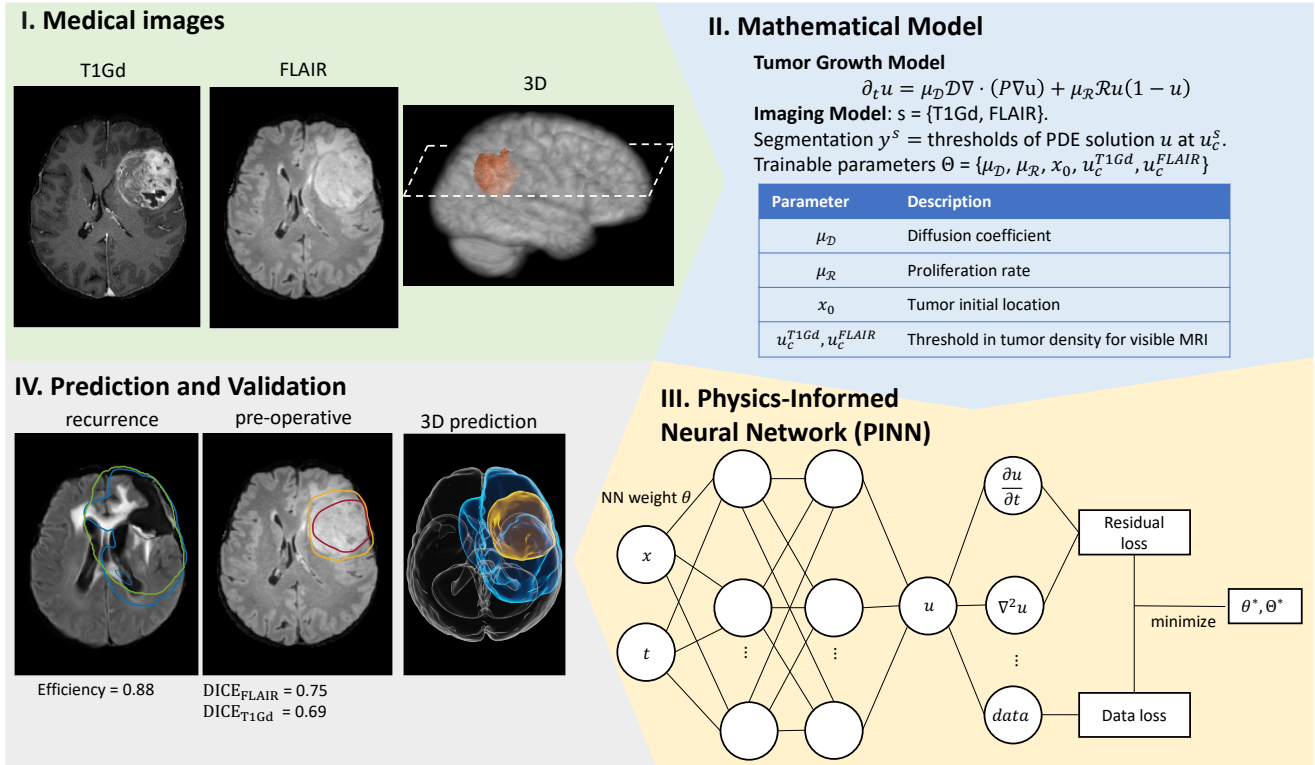


Fig. 1: Overview of the parameter estimation framework. **I) Medical Images** show preoperative patient T1Gd and FLAIR scans. **II) Mathematical Model** includes a Partial Differential Equation (PDE) for the tumor cell density u , and an imaging model that relates medical images with u by thresholding (segmentation). The unknown parameters that need to be estimated are tabulated. **III) Physics-Informed Neural Network (PINN)** is used to solve the PDE and estimate parameters from data. See Fig. 2 below for a detailed workflow. **IV) Prediction and Validation:** The estimated parameters can be used in the PDE model to predict the 3D tumor cell density (right), and can be validated via DICE scores (center). Left: The personalized clinical target volume (CTV, blue) based on model predictions is compared with Radiation Therapy Oncology Group (RTOG) CTV (green) to evaluate radiation volume and coverage of tumor recurrence (efficiency).

arise near the ventricles, especially when there is significant deformation of the brain due to the tumor. It remains an active area of research to design registration methods that robustly account for significant distortions due to tumor mass effect and post-surgical resection (Lipková et al., 2019). While we used a single brain atlas here, we could have used multiple atlases and chosen the atlas for registration that most closely matched the patient scans (Subramanian et al., 2023). We assume the initial condition is $u_0(\mathbf{x}) = 0.1 \exp(-0.1|\mathbf{x} - \mathbf{x}_0|^2)$, where \mathbf{x}_0 denotes the initial location of the tumor.

2.1.2. Diffuse Domain Method

A common way of enforcing the boundary condition using PINN requires sampling collocation points on the exact location of the boundary. However, the brain geometry is complex and the image resolution is limited, therefore an exact parameterization and the normal vector field of the boundary is not easily obtainable. In our work, the boundary condition is handled by

the diffuse domain method (Lervåg and Lowengrub, 2015; Li et al., 2009), which embeds the complex brain region Ω into a cubic box Ω_B by using a phase field function ϕ that replaces the sharp boundary of the domain with a smooth transition layer, and the PDE is modified:

$$\frac{\partial}{\partial t}(\phi u) = D \nabla \cdot (P \phi_\tau \nabla u) + \phi \rho u (1 - u) \quad \text{in } \Omega_B, \quad (3)$$

where $\phi_\tau = \phi + \tau$ and $\tau > 0$ is small. This PDE can be solved in Ω_B , with a uniform discrete mesh set by the MRI image resolution (1mm in our case). The boundary condition for u in the extended domain Ω_B can be Dirichlet, Neumann, or periodic, as long as the computation boundary is far away from the brain boundary Ω . The phase field function ϕ can be obtained by evolving the Cahn-Hilliard Equation for a short period of time:

$$\begin{cases} \frac{\partial \phi}{\partial t} = \nabla \cdot ((\phi(1 - \phi)) \cdot \nabla (g'(\phi) - \epsilon^2 \Delta \phi)) & \text{on } \Omega_B \\ \phi = 0 & \text{on } \partial \Omega_B \\ \phi = 1_\Omega & \text{at } \{t = 0\} \end{cases} \quad (4)$$

where $g(\phi) = \phi^2(1 - \phi)^2/4$ is a double-well potential, and ϵ is the width of the diffuse interface, chosen to be 3mm here. In our work, we solve (4) and (3) using a finite difference method (FDM) with standard central difference scheme and explicit Euler time stepping.

2.1.3. Scaling

The MRI image shows the thresholded tumor cell density at an unknown time t_{end} . It is impossible to infer $(D, \rho, t_{\text{end}})$ simultaneously from a single time point: doubling the time and halving D and ρ will give the same solution. In Konukoglu et al. (2010b); Ezhov et al. (2023, 2022b), time-independent parameters $\sqrt{Dt_{\text{end}}}$ and $\sqrt{\rho t_{\text{end}}}$ are considered, and they suffice to predict the tumor cell density and infiltration pattern at the unknown time of imaging. Additional information regarding the time scale would be needed to determine the precise values of $(D, \rho, t_{\text{end}})$.

In this work, we apply the idea from (Konukoglu et al., 2010b; Ezhov et al., 2023), but with a different scaling technique. Let \bar{D} and $\bar{\rho}$ be characteristic values of the diffusion coefficient and proliferation rate. Then, we can define the characteristic velocity $\bar{v} = \sqrt{\bar{D}\bar{\rho}}$. Given a length scale \bar{L} , we can define a characteristic time $\bar{T} = \bar{L}/\bar{v}$.

We can then define non-dimensional characteristic parameters \mathcal{D} and \mathcal{R} :

$$\mathcal{D} = \frac{\bar{D}\bar{T}}{\bar{L}^2}, \quad \mathcal{R} = \bar{\rho}\bar{T}. \quad (5)$$

We also define the ratios of the diffusion coefficient and proliferation rate with respect to their characteristic values as

$$\mu_{\mathcal{D}} = \frac{D}{\bar{D}} \frac{t_{\text{end}}}{\bar{T}}, \quad \mu_{\mathcal{R}} = \frac{\rho}{\bar{\rho}} \frac{t_{\text{end}}}{\bar{T}}, \quad (6)$$

By scaling the equation with $\bar{t} = t/t_{\text{end}}$, $\bar{x} = x/\bar{L}$, we obtain the non-dimensional equation

$$\frac{\partial u}{\partial \bar{t}} = \mu_{\mathcal{D}} \mathcal{D} \nabla \cdot (P\phi \nabla u) + \mu_{\mathcal{R}} \mathcal{R} \phi u (1 - u), \quad (7)$$

We also define the patient-specific characteristic solution \bar{u} as the solution of the PDE with $\mu_{\mathcal{D}} = \mu_{\mathcal{R}} = 1$.

From our definitions, we have $\mathcal{D} = \sqrt{\bar{D}/\bar{\rho}}/\bar{L} = 1/\mathcal{R}$. Therefore \bar{L} and $\bar{D}/\bar{\rho}$ completely determine \mathcal{D} , \mathcal{R} , and hence \bar{u} accordingly. We can use a grid search procedure to estimate \bar{L} and

$\bar{D}/\bar{\rho}$ for each patient, which makes the characteristic parameters, and solution, patient-specific. The estimation uses a surrogate model in a spherically symmetric geometry (see Sec 2.2). If our estimation of \mathcal{D} and \mathcal{R} is accurate, then we would expect $\mu_{\mathcal{D}}$ and $\mu_{\mathcal{R}}$ to be around 1. Therefore instead of trying to learn parameters of different magnitudes, we instead learn parameters that are of order 1, which enhances the efficiency of the training algorithm. In addition, the patient-specific characteristic solution \bar{u} is an excellent starting point for the PINN to learn patient specific parameters ($\mu_{\mathcal{D}}$, $\mu_{\mathcal{R}}$, etc.). Therefore, we use the FDM to obtain \bar{u}^{FDM} , the FDM approximation of \bar{u} , and use \bar{u}^{FDM} to pre-train the PINN. This will be discussed in Sec. 2.2. Because it is very efficient to obtain the patient-specific characteristic solution \bar{u}^{FDM} (e.g., 1-2 minutes of computation time), we tested whether \bar{u}^{FDM} itself provides a good approximation of the tumor cell density. We found that while the approximation using \bar{u}^{FDM} is surprisingly good, the fine-tuning step significantly improves accuracy (see Appendix D, Table D.5 and Fig. D.16).

2.1.4. Multimodal Imaging Model

We consider binary segmentations obtained from T1Gd, which highlights the tumor core, and FLAIR, which highlights the edema region in addition to the tumor core (Lê et al., 2016; Lipková et al., 2019; Subramanian et al., 2020b; Tunc et al., 2021; Menze et al., 2011; Ezhov et al., 2023; Konukoglu et al., 2010a). Let y^{T1Gd} be the indicator function of the tumor core and y^{FLAIR} be the indicator function of the tumor core and edema region. We assume that the y^{T1Gd} and y^{FLAIR} are related to the tumor cell density u through thresholding at u_c^{T1Gd} and u_c^{FLAIR} respectively, that is, for $s \in \{\text{T1Gd}, \text{FLAIR}\}$

$$y^s(\mathbf{x}) = \mathbb{1}_{\{u(\mathbf{x}) > u_c^s\}} \quad (8)$$

Following Lipková et al. (2019), we can also incorporate the 18-fluoride-fluoro-ethyl-tyrosine positron emission tomography (FET-PET) signal as additional data in the inference process. The FET-PET signal measures the metabolic activity of the tumor cells and is positively correlated to the tumor cellularity (Stockhammer et al., 2008; Hutterer et al., 2013). However, FET-PET (hereafter referred to as FET) is not routinely

available in the clinic. Let p be the normalized FET signal obtained by subtracting the patient-specific background activity, thresholding and normalizing to $[0,1]$, and y^{FET} be the indicator function of the region with positive FET signal. We assume that, in the region with positive normalized FET signal, there is a linear relationship between p and u :

$$p(\mathbf{x}) = (mu(\mathbf{x}) - A)y^{\text{FET}}(\mathbf{x}), \quad (9)$$

where the intercept A and the slope m are patient-specific and unknown. In Lipková et al. (2019), FET was found to be important to obtain accurate tumor cell density predictions. Here, we show that FET is not necessary in our method.

2.2. Workflow

This section outlines the step-by-step workflow of our parameter estimation process, as visualized in Fig. 2. In the pre-processing step, we first register the atlas to the patient T1Gd and obtain the geometry $P(\mathbf{x})$, and solve Eq. (4) to obtain the phase field function ϕ . Next from the segmentation, we compute the centroid of the tumor core, and the maximum radii of y^{FLAIR} and y^{T1Gd} , denoted as $R_{\text{seg}}^{\text{FLAIR}}$ and $R_{\text{seg}}^{\text{T1Gd}}$, which serve as features from the images.

Next, we estimate the characteristic parameters $\bar{D}/\bar{\rho}$ and \bar{L} by a grid search procedure. If we ignore the complex geometry of the brain, i.e. $P(\mathbf{x}) = 1$, then in spherical coordinates the characteristic PDE reduces to a one-dimensional equation $\bar{u}^{\text{sph}}(r, t)$ with Neumann boundary conditions, which can be solved easily:

$$\frac{\partial \bar{u}^{\text{sph}}}{\partial t} = \mathcal{D} \frac{1}{r^2} \frac{\partial}{\partial r} \left(r^2 \frac{\partial}{\partial r} \bar{u}^{\text{sph}} \right) + \mathcal{R} \bar{u}^{\text{sph}} (1 - \bar{u}^{\text{sph}}) \quad (10)$$

For samples in $\bar{D}/\bar{\rho} \in [0.1, 1]$ and $\bar{L} \in [10, 90]$ (which generate spherical tumors with radii smaller than 120mm), we solve the simplified PDE to find the radii $R_{\text{sph}}^{\text{FLAIR}}$ and $R_{\text{sph}}^{\text{T1Gd}}$ at which the tumor cell density is equal to characteristic values of the thresholds, which are taken to be $\bar{u}_c^{\text{FLAIR}} = 0.35$ and $\bar{u}_c^{\text{T1Gd}} = 0.6$, respectively, motivated by results in Lipková et al. (2019). The pair of $\bar{D}/\bar{\rho}$ and L that results in $R_{\text{sph}}^{\text{FLAIR}}$ and $R_{\text{sph}}^{\text{T1Gd}}$ that are closest to $R_{\text{seg}}^{\text{FLAIR}}$ and $R_{\text{seg}}^{\text{T1Gd}}$ will be used as the characteristic parameters. The details of this procedure are given in Appendix E. This procedure is very fast as the PDE is one-dimensional,

independent of the patient data, and the quantities $R_{\text{sph}}^{\text{FLAIR}}$ and $R_{\text{sph}}^{\text{T1Gd}}$ can be precomputed and stored as a look-up table. In addition, we do not need to perform a very refined grid search, because the actual parameters will be fine-tuned by the PINN with patient data.

With the patient specific \mathcal{D} and \mathcal{R} , we can solve the original PDE (7) with $\mu_{\mathcal{D}} = \mu_{\mathcal{R}} = 1$ using the FDM in the patient's geometry to obtain the characteristic solution \bar{u}^{FDM} . We then train the PINN to approximate \bar{u}^{FDM} . We call this step pre-training as it prepares the PINN for estimating the patient-specific parameters by initializing the weights of the PINN so that the PINN approximates a PDE solution instead of being a random function without PDE structure. In our experience, this makes the training process much more efficient and robust.

In the final stage, we use the segmentation data to fine-tune the weights of the PINN and learn the patient specific parameters $\mu_{\mathcal{D}}$ and $\mu_{\mathcal{R}}$. These estimated parameters can be used for tumor predicting the tumor cell densities.

2.3. Loss functions

In this section, we define the loss functions for pre-training and fine-tuning of the PINN. For notational simplicity, let $u(\mathbf{x}, t)$ denote the function represented by the PINN, with x and t already normalized. To enforce the initial condition, we set $u(\mathbf{x}, t) = tu^{\text{NN}}(\mathbf{x}, t) + u_0(\mathbf{x})$, where u^{NN} is a fully connected neural network. Define the differential operator \mathcal{F} of the PDE (7) as

$$\mathcal{F}[u] = \mu_{\mathcal{D}} \mathcal{D} \left(\nabla(P\phi) \cdot \nabla u + P\phi \nabla^2 u \right) + \mu_{\mathcal{R}} \mathcal{R} \phi u (1 - u) - \frac{\partial u}{\partial t} \quad (11)$$

Here we write the PDE in non-divergence form, since the geometry $P\phi$ and its gradient $\nabla(P\phi)$, which is approximated by finite differences using data from the pixels in the MRI scans, are known data.

Let $\{\mathbf{x}_i^r, t_i\}_{i=1}^{N_r}$ be the collocation points for the residual loss function. The residual loss function is defined as

$$\mathcal{L}_{\text{PDE}} = \frac{1}{N_r} \sum_{i=1}^{N_r} (\mathcal{F}[u](\mathbf{x}_i^r, t_i))^2, \quad (12)$$

Because the solution is changing rapidly at early times and the tumor grows from the center, we sample the collocation points

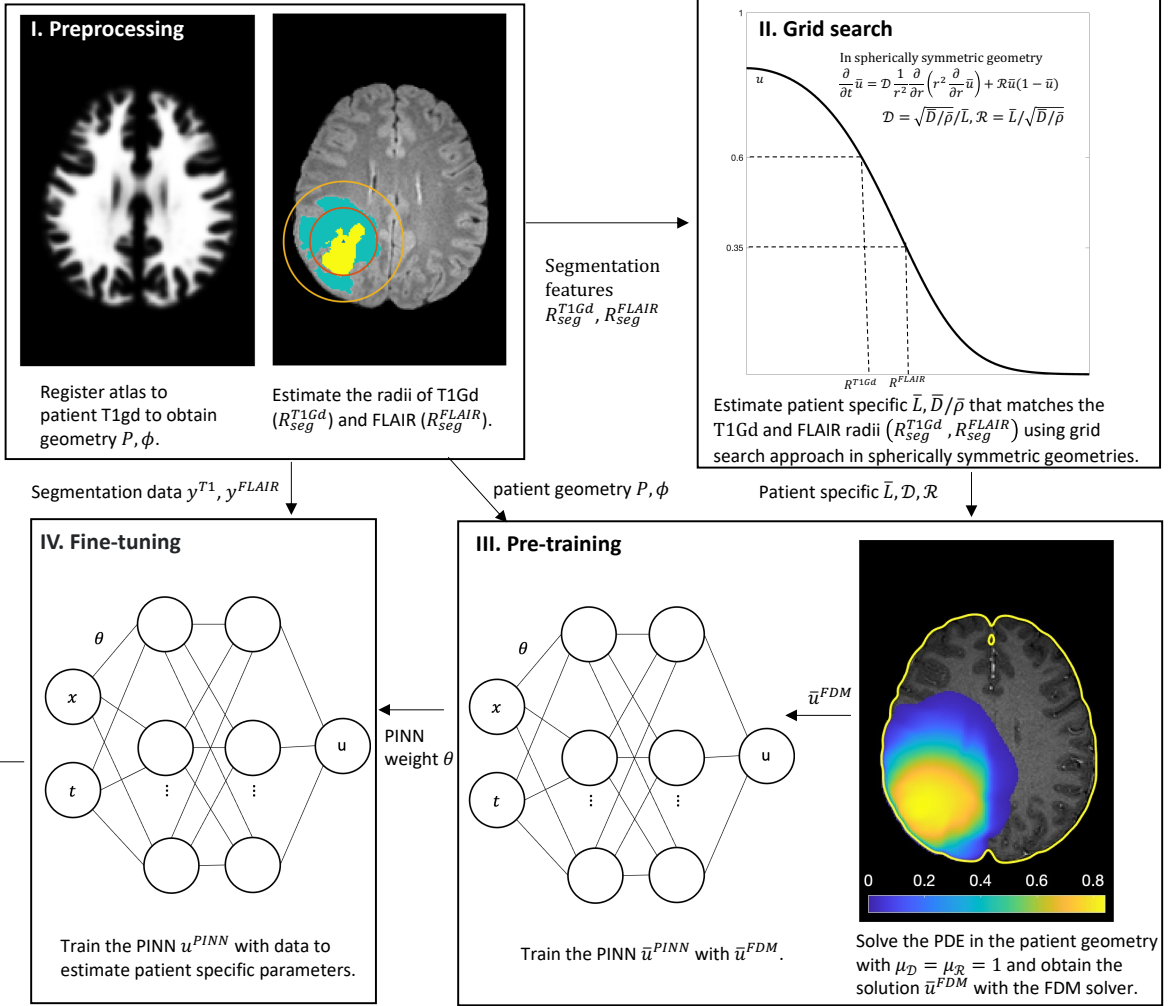


Fig. 2: Workflow for patient-specific parameter estimation via PINN. **I. Preprocessing:** Register the brain atlas to the T1Gd patient scan. Solve the Cahn-Hilliard equation to acquire the geometry. Compute centers and radii of T1Gd and FLAIR segmentations ($R_{\text{seg}}^{\text{T1Gd}}$ and $R_{\text{seg}}^{\text{FLAIR}}$). **II. Grid Search:** In a spherically symmetric geometry, use a grid search algorithm to identify patient-specific characteristic values of $\bar{D}/\bar{\rho}$ and L such that the radii derived from the PDE solution are close to $R_{\text{seg}}^{\text{T1Gd}}$ and $R_{\text{seg}}^{\text{FLAIR}}$. **III. Pre-training:** Solve the PDE using a Finite Difference Method (FDM) with the patient-specific characteristic parameters (and $\mu_D = \mu_R = 1$) in the patient geometry to obtain a characteristic solution \bar{u}^{FDM} . Train the PINN to solve the PDE using \bar{u}^{FDM} as data. **IV. Fine-Tuning:** Use the segmentation data to fine-tune the PINN and learn the patient specific parameters μ_D and μ_R . These estimated parameters are used for tumor cell density predictions.

for PDE loss densely at early times and in the center of the tumor. This was found to work better than other spatial distributions of the collocation points, including adaptive sampling (Lu et al., 2021b) (see Appendix B for details).

To facilitate training of the characteristic PINN, we also minimize the Mean Squared Error (MSE) with respect to the characteristic solution \bar{u}^{FDM}

$$\mathcal{L}_{\text{char}} = \frac{1}{N_r} \sum_{i=1}^{N_r} \left(\phi(\mathbf{x}_i^r) u(\mathbf{x}_i^r, t_i) - \phi(\mathbf{x}_i^r) \bar{u}^{\text{FDM}}(\mathbf{x}_i^r, t_i) \right)^2. \quad (13)$$

Thus the total loss function for pre-training is

$$\mathcal{L}_{\text{total}} = \mathcal{L}_{\text{PDE}} + \mathcal{L}_{\text{char}}. \quad (14)$$

For fine-tuning the PINN, we replace $\mathcal{L}_{\text{char}}$ by loss functions

based on the imaging data. Let $\{\mathbf{x}_i^{\text{dat}}\}_{i=1}^{N_{\text{dat}}}$ be the spatial collocation points for the data loss. Note that all the imaging data are provided at the normalized time $t = 1$. The points \mathbf{x}^{dat} are sampled uniformly at pixel resolution. We define the predicted segmentation obtained by thresholding the cell density at u_c^s :

$$H_{u_c^s}(x) = [1 + \exp\{-a(\phi(\mathbf{x})u(\mathbf{x}, 1) - u_c^s)\}]^{-1} \quad (15)$$

which is a smoothed heaviside function in $[0,1]$ (we set $a = 20$). The segmentation loss function is defined as

$$\begin{aligned} \mathcal{L}_{\text{SEG}} = \frac{1}{N_{\text{dat}}} \sum_{i=1}^{N_{\text{dat}}} & \left(H_{u_c^{\text{FLAIR}}}(\mathbf{x}_i^{\text{dat}}) - y^{\text{FLAIR}}(\mathbf{x}_i^{\text{dat}}) \right)^2 + \\ & \left(H_{u_c^{\text{T1Gd}}}(\mathbf{x}_i^{\text{dat}}) - y^{\text{T1Gd}}(\mathbf{x}_i^{\text{dat}}) \right)^2 \end{aligned} \quad (16)$$

where u_c^{FLAIR} and u_c^{T1Gd} are trainable parameters. If the FET data is used, the loss function for FET signal is defined as

$$\mathcal{L}_{\text{FET}} = \frac{1}{N_{\text{dat}}} \sum_{i=1}^{N_{\text{dat}}} \left(m\phi(\mathbf{x}_i^{\text{dat}})u(\mathbf{x}_i^{\text{dat}}, 1) - A - p(\mathbf{x}_i^{\text{dat}}) \right)^2 y^{\text{FET}}(\mathbf{x}_i^{\text{dat}}) \quad (17)$$

where m and A are trainable parameters.

In the fine tuning stage, we also restrict the range of the trainable parameters: $\mu_{\mathcal{D}} \in [0.75, 1.25]$, $\mu_{\mathcal{R}} \in [0.75, 1.25]$, $u_c^{\text{FLAIR}} \in [0.2, 0.5]$, $u_c^{\text{T1Gd}} \in [0.5, 0.8]$, $m \in [0.8, 1.2]$, $A \in [0, 1]$. As discussed earlier, we expect $\mu_{\mathcal{D}}$ and $\mu_{\mathcal{R}}$ to be close to 1. The ranges for other parameters are based on the priors in (Lipková et al., 2019). The constraints are enforced by adding the quadratic penalty losses: if a parameter $\beta \in [\beta_{\min}, \beta_{\max}]$, then

$$\mathcal{L}_{\beta} = \min(0, \beta - \beta_{\min})^2 + \max(0, \beta - \beta_{\max})^2 \quad (18)$$

In all, the total loss for fine-tuning with segmentation and FET data (if used) is

$$\mathcal{L}_{\text{total}} = \mathcal{L}_{\text{PDE}} + w_{\text{SEG}} \mathcal{L}_{\text{SEG}} + w_{\text{FET}} \mathcal{L}_{\text{FET}} + \sum_{\beta \in \Theta} \mathcal{L}_{\beta}, \quad (19)$$

where $\Theta = \{\mu_{\mathcal{D}}, \mu_{\mathcal{R}}, \mathbf{x}_0, u_c^{\text{FLAIR}}, u_c^{\text{T1Gd}}, m, A\}$ are trainable parameters, and w_{SEG} and w_{FET} are the weights of the segmentation and FET loss respectively. If FET data is not used, then $w_{\text{FET}} = 0$. In this work we set $w_{\text{SEG}} = 1e-3$ and $w_{\text{FET}} = 1e-2$ if FET data is used, while all the other losses have unit weights. These weights are chosen such that the losses are of similar magnitude, such that the training is not dominated by one particular loss. Although we tried other choices of the weights, including adaptively changing them in time (Groenendijk et al., 2020; Maddu et al., 2022; Chen et al., 2018; Wang et al., 2021), we found empirically that this choice of weights works well for all our numerical experiments. See Appendix A for details on training the neural network and for examples of the dynamics of loss functions during training. See Appendix F for different choices of the data loss.

3. Results

We start by presenting an overview of the results and our findings. In this work we use 3 different datasets, including data from 24 patients, to test and validate our approach:

- Synthetically-generated data, denoted as S1-S8: We specify the ground truth (GT) parameters, solve the PDE by the FDM to obtain the cell density, add spatially correlated noise to the density, and generate synthetic segmentations and FET distributions.
- Data from 8 patients (P1-P8), primary tumors and first detected recurrence, from (Lipková et al., 2019). All the patients have T1Gd and FLAIR scans at recurrence.
- Data from 16 patients (Q1-Q16), primary and first detected recurrence, from the Klinikum Rechts Der Isar repository. At recurrence, patients Q1-Q3 have both T1Gd and FLAIR scans, the others only have T1Gd scans.

We test parameter estimation using segmentations of T1Gd and FLAIR scans and FET-PET (denoted as **FET+SEG**), and using segmentations alone (denoted as **SEG**). The difference between the two lies in the loss functions used in the fine-tuning stage: **FET+SEG** includes the FET loss \mathcal{L}_{FET} , in addition to the segmentation loss \mathcal{L}_{SEG} .

We demonstrate that using segmentation alone achieves results comparable to those using segmentation and FET, in contrast to the results in (Lipková et al., 2019) where FET was needed to more accurately determine spatial distributions of the cells, particularly near the tumor center. This finding is noteworthy as FET-PET data is not widely available from the clinic, thereby accentuating the practicality of our approach.

Furthermore, we examine two methods to predict cell density after fine-tuning: u^{FDM} , derived from solving the PDE with estimated parameters using the FDM, and u^{PINN} , obtained by evaluating the PINN. We show that u^{FDM} is more accurate in terms of solving the PDE as u^{PINN} is influenced by the noisy data via the loss function. Additionally, the FDM can be used to solve the PDE to any non-dimensional time. However, extending the PDE solution to future times with the PINN requires re-sampling and extending the collocation points, and retraining the network with the PDE loss, which tends to be more time consuming.

3.1. Synthetic data

Figure 3 presents detailed results for a synthetic tumor (labeled S5); the ground truth and inferred parameters are shown in Table C.2. The results for the other synthetic tumors are shown in the Supplementary Material. The first row shows the Ground Truth (GT) data: 3D isosurfaces of tumor cell density at 1% and 30%, cell density, synthetic segmentation, and synthetic FET signal. The synthetic cell density, denoted as u^{GT} , is obtained by solving the PDE with the GT parameters (μ_D, μ_R, x_0) using the FDM (the results would be similar if we solve the PDE using the PINN). The synthetic segmentation is obtained by thresholding u^{GT} at u_c^{T1Gd} and u_c^{FLAIR} . The synthetic FET signal is formulated as $p = (mu^{GT} - A)y^{FET}$, and y^{FET} is the region where $mu^{GT} - A > 0$. The second row presents the training data generated by introducing spatially correlated noise to the GT, (see Appendix C and Figure C.13 for further details of the noise). The segmentations from the noise-perturbed solutions deviate noticeably from the GT. In the third and fourth rows, we show the results of **FET+SEG** using u^{PINN} in row 3 and u^{FDM} , with the estimated parameters, in row 4. Although the inferred segmentations for the PINN (dashed, Fig. 3(k)) are closer to the ground truth than for the FDM (solid, Fig. 3(o)), the cell density predicted by u^{FDM} overall is a better fit to the ground truth data than is u^{PINN} (the MSEs for u^{FDM} and u^{PINN} are 3.8×10^{-5} and 1.4×10^{-4} , respectively). This is because the PINN is more influenced by the noisy data via the data loss term in the loss function. Therefore u^{FDM} will be used for our predictions. Comparing the fourth and fifth rows, the estimated cell density using **FET+SEG** is very similar to that using **SEG** alone, with both being close to the GT because the estimated parameters are accurate (Appendix C Table C.2). As **SEG** simulations do not provide estimated FET signals, Figure 3(t) directly compares the contours of u^{FDM} using **SEG** with GT contours at 1%, 25%, 50%, and 75%, and shows there is very good agreement with the ground truth data.

The PDEs with the inferred parameters can be used to predict tumor evolution at arbitrary times, before or after the time of imaging. Directly evaluating the PINN at time beyond the

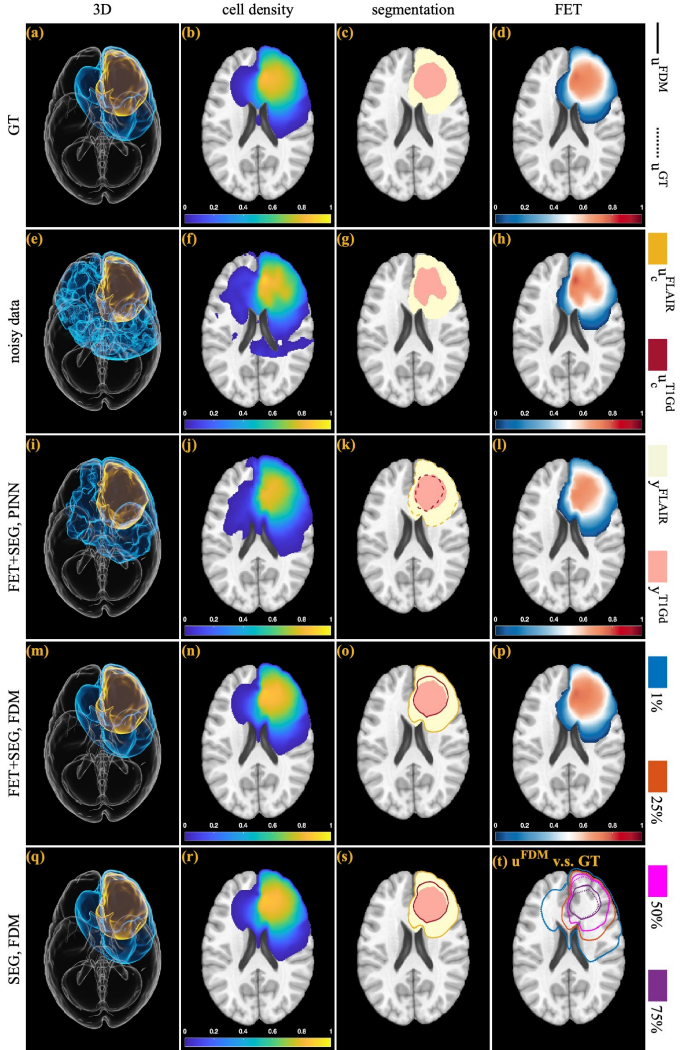


Fig. 3: Validation using synthetic data. Row 1: (a)-(d). ground truth (GT) data; Row 2: (e)-(h). Training data— GT with correlated noise; Row 3: (i)-(l). Parameter estimation using noisy, synthetic **FET+SEG** data and predictions by evaluating the PINN solution, u^{PINN} ; Row 4: (m)-(p). Parameter estimation using noisy **FET+SEG** data and predictions using the FDM solution of the PDE, u^{FDM} , with inferred parameters; Row 5: (q)-(t). Parameter estimation using only the noisy **SEG** data and predictions using u^{FDM} . (t): Comparison of contours at 1%, 25%, 50%, and 75% between u^{FDM} (solid) and GT u (dotted). Column 1: 3D isosurfaces of tumor cell density at 1% and y^{FLAIR} ; Column 2: Cell densities; Column 3: Synthetic segmentations mimicking T1Gd and FLAIR data; Column 4: Synthetic FET-PET distributions. Further, (k), (o) and (s) show comparisons of predicted segmentations (lines—dashed, solid) with GT segmentations (filled). Comparing rows 3 and 4, u^{PINN} is less accurate than u^{FDM} as a solution of the PDE with the inferred parameters because u^{PINN} is more strongly influenced by the noisy data. Notably, the estimated cell densities from the u^{FDM} using **FET+SEG** and **SEG** in rows 4 and 5, respectively, are very similar and yield accurate approximations of the GT data.

range of the temporal domain used in training tends to yield poor results, although this can be remedied by re-sampling collocation points and re-training the network with the PDE loss, or by novel methods to enhance the extrapolation capabilities of PINN (Kim et al., 2020). It should be noted that our method only permits the use of normalized time as the time scale re-

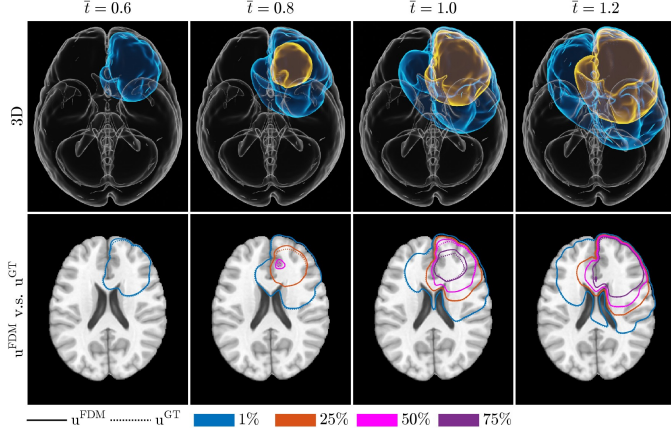


Fig. 4: Predicted tumor morphologies at times different from that of training data. Morphologies are shown at the normalized times $\bar{t} = 0.6, 0.8, 1.0, 1.2$, and are obtained using u^{FDM} with parameters inferred from the synthetic data in Fig. 3. Only **SEG** data is used for inference and the training data corresponds to the normalized time $\bar{t} = 1$. Row 1: 3D isosurfaces of u^{FDM} at 1% and 30%. Row 2: Comparison of predicted contours (solid; 1%, 25%, 50% and 75%) with GT (dotted).

mains unknown. Figure 4 demonstrates the predicted dynamics of tumor cell density u^{FDM} at normalized times $\bar{t} = 0.6, 0.8, 1.0, 1.2$, with data provided at $\bar{t} = 1$. The first row shows the 3D isosurfaces of u^{FDM} at 1% and 30%. The second row shows the predicted contours and those of the GT. The predicted dynamics of tumor growth align closely with the GT because the estimated parameters are close to the GT parameters.

3.2. Patient tumors

In this section, our method is applied to data from 24 patients: P1-P8 and Q1-Q16. As an example, Figure 5 demonstrates the results of the inference for patient P5 using **SEG** and **FET+SEG** as data. The estimated parameters are given in Table D.4. The first row presents the preoperative scans (a) T1Gd (b) FLAIR, (c) the pre-processed FET (as described in 2.1.4) and (d) the original FET data. The second and third rows exhibit the results for u^{FDM} using **FET+SEG** and **SEG** data, respectively. Upon comparing columns 1, 2, and 4, it is evident that the estimations using **FET+SEG** and **SEG** result in similar predicted tumor cell densities, and the predicted segmentations align closely with the actual segmentations. The Radiation Therapy Oncology Group (RTOG) Clinical Target Volume (CTV), denoted as CTV^{RTOG} , is defined as the 2 cm margin around the FLAIR segmentation (Gilbert et al. (2013)). The personalized CTV, denoted as CTV^P , is defined by threshold-

ing the predicted tumor cell density at $u^{FDM} = 1\%$ across all patients (blue contours in Figs. 5 (f) and (j)). This threshold was selected so that the efficiency of the CTV^P is comparable to that of the CTV^{RTOG} (green contours in Figs. 5 (f) and (j)). Figures 5(f) and (j) reveal that both CTV^P and CTV^{RTOG} encompass the visible tumor, although CTV^P is smaller in size compared to CTV^{RTOG} . In Figure 5(g), the predicted FET signal using the **FET+SEG** data is displayed, and is highly correlated with the actual FET signal (see Appendix D Table D.4).

Figure 5(k) compares the contours of u^{FDM} (solid) and u^{PINN} (dashed) using **SEG** data. A comparison of density distributions is shown in Appendix D Fig. D.14. As observed in the synthetic data, the predicted segmentation from u^{PINN} aligns more closely with the actual segmentation than u^{FDM} does, while the 1% contour is somewhat noisier than that from u^{FDM} . However, a close alignment with the actual segmentation is not necessarily advantageous as it suggests that u^{PINN} is fitting the data rather than effectively solving the PDE. This behavior is inherent in the PINN as the PDE loss merely imposes a soft constraint on the PINN. In particular, when the model cannot fully account for the data, PINN might sacrifice the PDE loss to fit the data, as long as the total loss is reduced. Our synthetic data experiments indicate that even though u^{PINN} at time 1 is influenced by the noise, the estimated parameters remain reliable. Therefore, despite the absence of a ground truth with patient data, we advocate for the use of u^{FDM} for predictions, as it solves the PDE without being swayed by the noise and the PDE errors, and provides less noisy segmentations and 1% contours, which are important for predicting infiltration.

As in the synthetic data case, the evolution of patient tumors in normalized time can be studied. Fig. 6 shows a 3D visualization of the predicted dynamics of the tumor growth u^{FDM} from patient P5 at normalized times $\bar{t} = 0.6, 0.8, 1.0, 1.2$ (recall that the data is provided at $\bar{t} = 1$).

Figure 7 shows the results for patients P1-P8 using **SEG** data. The estimated model parameters can be found in Appendix D Table D.4. The T1Gd and FLAIR images are shown in Figs. 7 (A) and (B), and the predictions are shown in Figs. 7 (C-F).

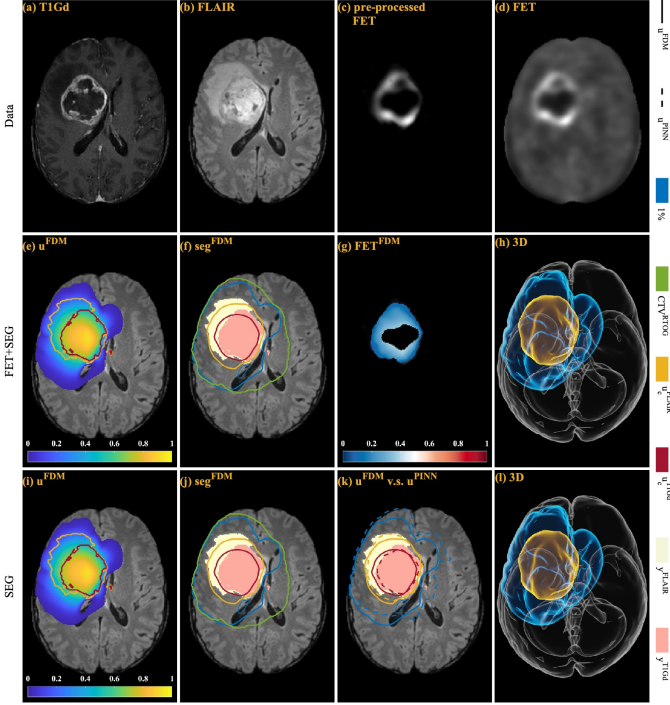


Fig. 5: Predicted patient-specific tumor morphologies, cell densities and FET-PET distributions from Patient 5 (see text). Row 1: Medical images: (a) T1Gd; (b) FLAIR; (c) Post-processed FET-PET (see text); (d) Original FET-PET data. Row 2: u^{FDM} predictions using **FET+SEG** data. Row 3: u^{FDM} predictions using **SEG** data only. (e) and (i): Predicted cell density distributions from u^{FDM} together with boundaries of the segmentations (curves) from the MRI images. (f) and (j): Comparisons of the contours of u^{FDM} at the inferred segmentation thresholds (curves) with MRI segmentations (filled). Margins for CTV^{RTOG} (green) and CTV^P (blue); (g) predicted FET-PET distribution (see text). (h) and (l): 3D visualization of 1% and u_c^{FLAIR} isosurfaces. (k) Comparison of 1%, u_c^{FLAIR} , and u_c^{T1Gd} contours of u^{FDM} (solid) and u^{PINN} (dashed).

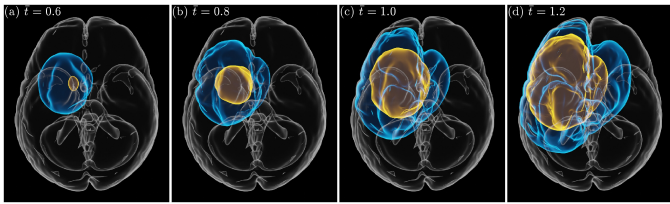


Fig. 6: Predicted dynamics of tumor from Patient 5 using the FDM at normalized times $\bar{t} = 0.6, 0.8, 1.0, 1.2..$ The data is provided at $\bar{t} = 1$. The 3D isosurfaces of u^{FDM} at 1% and 30% are shown.

All patients received standard treatment, which consists of immediate tumor resection, followed by combined radiotherapy and chemotherapy, and are monitored for recurrence regularly. Fig. 7 (e) shows the post-operative FLAIR scan with segmentations of the first detected tumor recurrences. The postoperative scans are registered to the preoperative T1Gd scans by rigid transformations (Lipková et al., 2019). The figures also plot the CTV^P (blue), indicative of the predicted tumor infiltration pathways, and CTV^{RTOG} (green) for comparison. All the CTV^P

and CTV^{RTOG} cover the recurrent tumor reasonably well. Further, for patient P5, CTV^P follows the contour of the recurrent tumor. For patient P8, we see infiltration into the other brain hemisphere beyond the CTV^P and CTV^{RTOG}. However, our predicted CTV^P seems to capture the infiltration pathway. The estimated parameters and the metrics, including DICE scores of the segmentations and correlations with FET signals, corresponding to Fig. 7 **SEG** are reported in Appendix D, Table D.4. The results of **FET+SEG** are reported in Appendix D, Fig. D.15 and Table D.4.

We consider another set of 16 patients Q1-Q16 and show the u^{FDM} results from parameter estimation using **SEG** in Figs. 9 and 10. The estimated parameters and metrics are tabulated in Appendix D, Table D.6. The results are consistent with patients P1-P8: estimations using **FET+SEG** data are very similar to those using **SEG** data. In Table 1, we compare the DICE scores and correlations with FET signals for all patients (24 in total) using characteristic parameters and parameters obtained by fine-tuning with **SEG** with **FET+SEG** data. Though the characteristic parameters yield good results, fine-tuning leads to better results, while the difference between using **FET+SEG** and **SEG** data is small. Additional results from the patient datasets are presented in Appendix D.

For a quantitative evaluation of the personalized CTVs, we follow Lipková et al. (2019) and use the CTV volume and efficiency of the CTV in capturing tumor recurrence as two criteria. A smaller CTV means that less healthy brain tissue is irradiated. The CTV efficiency is defined as the percentage of the recurrent tumor covered by the CTV:

$$\eta^{CTV} = |V^{REC} \cap V^{CTV}| / |V^{REC}|, \quad (20)$$

where V^{CTV} is the CTV region, V^{REC} is the FLAIR segmentation (tumor core and edema region) of the recurrent tumor and $|\cdot|$ denotes the volume. Figure 8 compares the volumes and efficiencies of RTOG CTV (blue) with the CTV^P (1% isosurface of predicted tumor cell density u^{FDM}) using different parameter inference results, **FET+SEG** (red), **SEG** (yellow), from patient data P1-P8 and Q1-Q3 for which we have both T1Gd and FLAIR images at recurrence. For patients P1-P8, we also

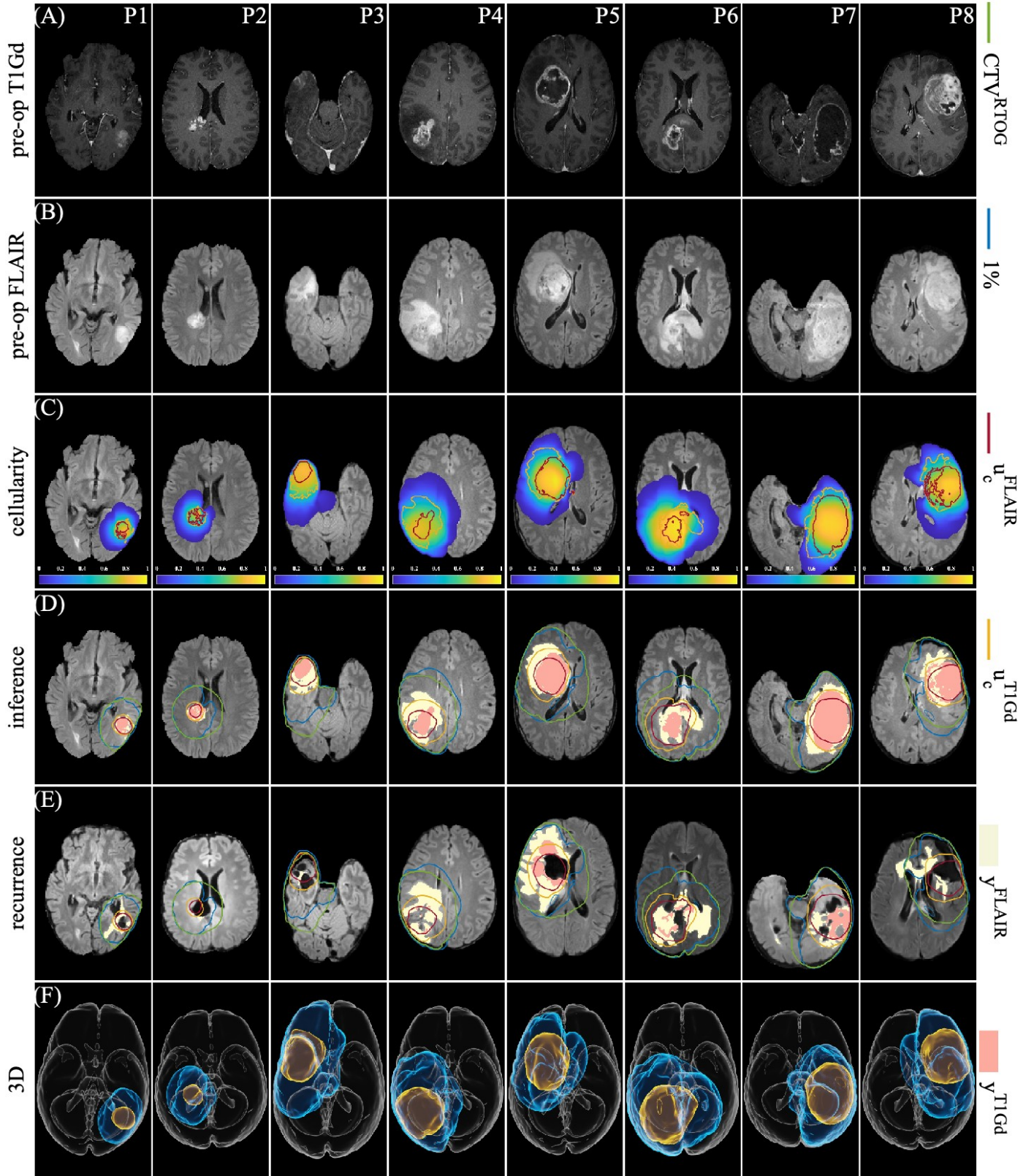


Fig. 7: Parameter Estimation Results for Patients P1-P8 using **SEG**. (a) Pre-operative T1Gd. (b) Pre-operative FLAIR. (c) Superposition of predicted tumor cell density u_c^{FDM} on actual segmentations: T1Gd (yellow line) and FLAIR (red line). (d) Overlap of inferred segmentations: u_c^{FLAIR} (yellow line) and u_c^{T1Gd} (red line) on actual segmentations: T1Gd (beige fill) and FLAIR (pink fill); Margins for CTV^{RTOG} (green) and CTV^P (blue). (e) Tumor recurrence, compared with with margins for CTV^{RTOG} (green) and CTV^P (blue). (f) 3D reconstructions of CTV^P and u_c^{FLAIR} isosurfaces. On average, pre-training took 37.9 (std 5.0) minutes, while fine-tuning was completed in 4.5 (std 0.1) minutes.

include the personalized CTVs based on the maximum a posteriori (MAP) estimates from Lipková et al. (2019) (purple).

The CTV^P volumes and efficiencies using **FET+SEG** and **SEG** data from our PINN-based inference are very similar and except for patients P2 and P8, where the volumes of the CTV^P from Lipková et al. (2019) are significantly smaller, the volumes and efficiencies using our PINN-based approach are similar to those from Lipková et al. (2019), which is much more expensive to compute. Compared to CTV^{RTOG}, the CTV^P from our study and from Lipková et al. (2019) exhibit reduced or similar volumes while maintaining efficiencies comparable to CTV^{RTOG}. Patient Q13 is an outlier, as the recurrent tumor has an exceptionally large edema region, leading to low efficiency for all CTVs. We discuss possible explanations for this in Appendix D and Fig. D.21.

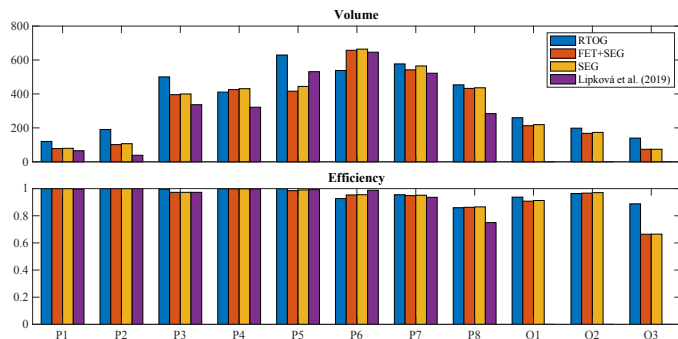


Fig. 8: Comparison of RTOG CTV (blue) with Personalized CTV (1% iso-surface of predicted tumor cell density) from different parameter inferences: Lipková et al. (2019) (purple), **FET+SEG** (red), and **SEG** (yellow). (A) Total irradiated volume. (B) Efficiency, a percentage tumor core and edema at the first detected recurrence that is covered by the CTV (see text). In general, the personalized CTV from Lipková et al. (2019), **FET+SEG**, and **SEG** present reduced or similar irradiation volumes while maintaining efficiency comparable to RTOG CTV.

	DICE ^{T1Gd}	DICE ^{FLAIR}	corr ^{FET}
Char	0.586(±0.123)	0.408(±0.183)	0.374(±0.201)
SEG	0.695(±0.091)	0.685(±0.160)	0.416(±0.224)
SEG+FET	0.695(±0.090)	0.686(±0.152)	0.421(±0.232)

Table 1: Average and standard deviation of DICE scores and correlation with FET signal for all 24 patients using characteristic parameters, or parameters obtained by fine-tuning with **SEG** with **FET+SEG** data. Fine-Tuning leads to better results.

3.3. Discussion

We briefly discuss the merits and limitations of our PINN approach, compared with other methods. One of the strengths

of Bayesian methods is their ability to quantify uncertainties, while PINNs provide deterministic outputs based on the minimizer of the loss function and do not inherently provide uncertainty estimates, although some methods have been proposed to integrate uncertainty quantification into PINNs (Yang et al., 2021). However, Bayesian methods are computationally expensive as they require solving the forward PDE problem many times to estimate the posterior distribution of the parameters, which might take up to days (Lipková et al., 2019; Ezhev et al., 2023). Our PINN implementation on TensorFLow (Abadi et al., 2015) takes about 30 min for the pre-training step and 5 min for the fine-tuning step on a single GPU (Nvidia Quadro RTX 8000).

Conventional PDE-constrained optimization methods, such as the adjoint method, are very efficient and solve the PDE using numerical solvers, which come with well-understood error estimators, as well as convergence and stability guarantees (Hogea et al., 2008; Gholami et al., 2016; Subramanian et al., 2020b,a, 2023). In contrast, the training of PINNs remains an active area of research (Karniadakis et al., 2021; Krishnapriyan et al., 2021; Wang et al., 2022b; Hao et al., 2023; Chen and Hao, 2022). One notable advantage of PINNs is their flexibility and simplicity in implementation: modifying the model primarily involves changing the loss function. In contrast, the adjoint method often requires derivation of the adjoint equation, careful regularization, and implementation of the adjoint solver, adding to the technical demands.

Another flexible machine learning approach, known as ODIL (Karnakov et al., 2022), was recently developed to estimate parameters of the Fisher-KPP PDE using MRI and FET-PET scans for GBM (Balcerak et al., 2023). Like the PINN, this method also minimizes a loss function that contains data and the PDE residual. In ODIL the residual of the PDE is calculated using a grid-based discretization of the PDE and the variables to be minimized are the solutions at the grid points in 4D (space+time) rather than weights of a neural network as in the PINN. Although the number of grid points can be very large, the multigrid method and the sparsity of the discrete systems

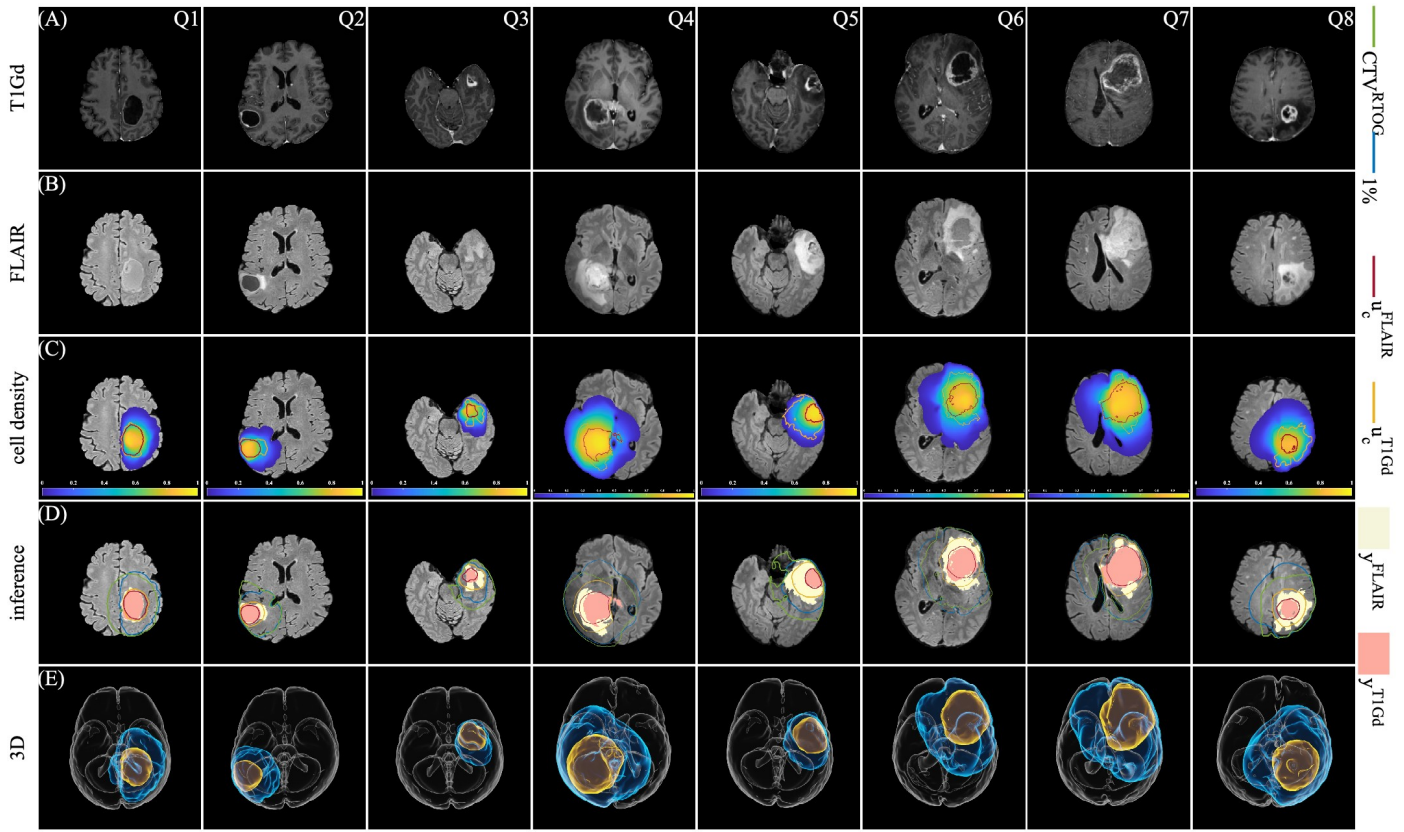


Fig. 9: Parameter Estimation Results for Patients Q1-Q8 using **SEG**. Recurrence results for Q1-Q3 are shown in Appendix D Fig .D.19. Legends are the same as 7. Results using **FET+SEG** are shown in Appendix D Fig. D.17.

can be used to improve efficiency. While promising, the current implementation uses downsampling of the medical images.

Another class of methods aims to learn the mapping between image and parameters directly, either by training a neural network (Ezhov et al., 2023), or by posing the inverse problem as a database query task (Ezhov et al., 2022b). These methods require a large number of forward PDE solves to generate a synthetic dataset and can take days to compute, which is generally not a concern in practice as it is done offline. The inference is extremely fast since it only requires evaluating the neural network or a for-loop search. In (Ezhov et al., 2023), 100,000 synthetic tumors were generated for training, while the inference was done in about 5 minutes. However, this approach does not allow any patient specific fine-tuning, thus might have larger errors if the patient data is significantly different from the training data.

Currently, our method requires pre-training for each patient using patient-specific characteristic parameters, obtained by

solving a 1D model in spherically symmetric geometries, and an associated patient-specific characteristic solution generated by solving the Fisher-KPP PDE with characteristic parameters in the patient brain geometry. From Table 1, we can see that the characteristic solution already gives remarkably effective predictions of tumor cell densities, as measured by DICE scores and correlations with FET-PET signals. This method works well because it incorporates insights into the tumor growth dynamics from image features, and solving the PDE in patient geometries captures the heterogeneity of the spreading. Fine-tuning with patient data is necessary to obtain more accurate results, but the improvement is also limited, because the Fisher-KPP equation is a simplified model that does not capture the full complexity of GBM growth, such as the mass effect or the presence of necrosis.

One might wonder if using an averaged set of the characteristic parameters can be used to pre-train a single network for all patients. We tested this (see Appendix H) and found that

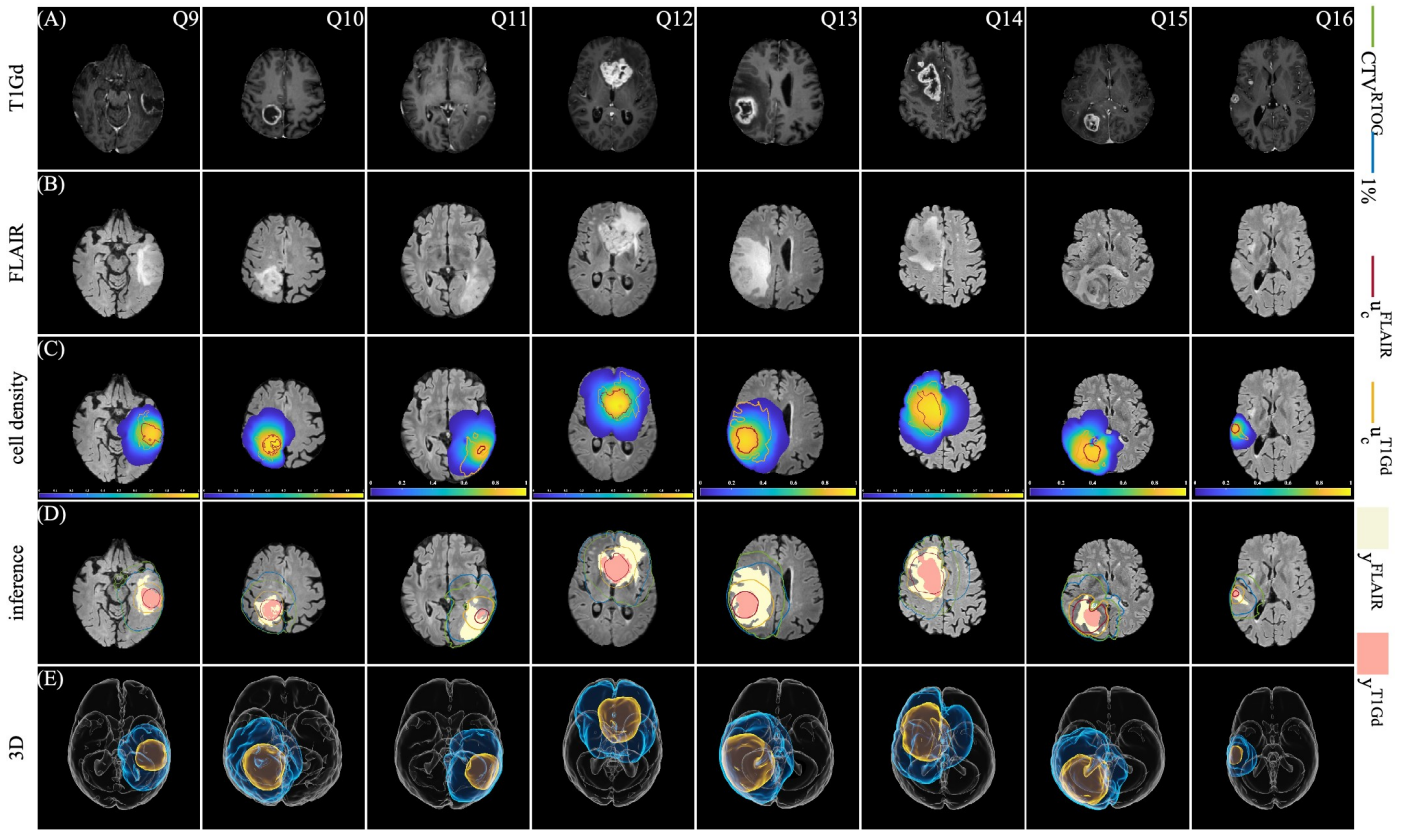


Fig. 10: Parameter Estimation Results for Patients Q9-Q16 using **SEG**. Legends are the same as 7. Results using **FET+SEG** are shown in Appendix D Fig. D.18.

such a pre-trained single network does not work well with our current framework because the tumors have different scales, as demonstrated by the wide range of patient-specific parameters. Without the patient-specific characteristic parameters, the pre-trained network can be far away from the solution, leading to difficulty in fine-tuning. Nevertheless, the idea of a common pre-trained network for all patients is appealing as it can significantly increase the inference speed. Consequently, in future work we will explore other approaches for developing a single network that can be used for all patients, including transfer learning (Xu et al., 2023; Desai et al., 2021; Gao et al., 2022) and neural operators (Li et al., 2020; Lu et al., 2021a)

4. Conclusion

We presented a method employing Physics-Informed Neural Networks (PINNs) to estimate patient-specific parameters of a reaction-diffusion PDE model for the growth of GBM tumors from a single snapshot of structural MRI scans. We applied a simple procedure to estimate patient-specific characteristic pa-

rameters of the PDE model using a 1D model in spherically symmetric geometries and a grid-search procedure. The characteristic parameters allowed us to scale the PDE to learn parameters that are close to unity, and helped us to pre-train the PINN to learn a characteristic solution before fine-tuning the network with patient data to estimate the patient-specific parameters, leading to a more efficient method. Verified on synthetic and patient datasets, the results presented here provide a proof-of-concept that PINNs hold great promise for combining medical images and biophysical models for patient-specific tumor growth prediction and treatment planning.

Declaration of competing interest

The authors declare that they have no known competing financial interests or personal relationships that could have appeared to influence the work reported in this paper

Data Availability

The pre-operative MRI scan of patient P1-P8 are available from Lipková et al. (2019). Other data will be made available on request. The PINN code is available at <https://github.com/Rayzhangzirui/pinn>

Acknowledgments

R.Z.Z and J.S.L thank Jana Lipkova, Peter Chang, and Xiaohui Xie for helpful discussions, and Babak Shahbaba for the GPU resources. J.S.L. acknowledges National Institutes of Health for partial support through grant nos. 1U54CA217378-01A1 for a National Center in Cancer Systems Biology at UC Irvine and P30CA062203 for the Chao Family Comprehensive Cancer Center at UC Irvine. In addition, J.S.L. acknowledges support from DMS-1763272, DMS-1936833, DMS-1953410, DMS-2309800 and the Simons Foundation (594598QN) for an NSF-Simons Center for Multiscale Cell Fate Research. BM and MB acknowledge support from the Helmut Horten Foundation.

Appendix A. Training of PINN

We use a fully connected neural network with 4 hidden layers. Each layer has 128 neurons, and the tanh activation function is used. Different training strategies are employed for pre-training and fine-tuning: Pre-training is done using the characteristic solution \bar{u}^{FDM} as data. We employed the ADAM optimizer with initial learning rate of 0.001, followed by L-BFGS-B optimizer with maximum number of variable metric corrections of 100, maximum number of line search steps of 50, and a tolerance for termination of 2.3e-09. We take $N_r = 20,000$. The loss is also computed on the same number of testing points. The maximum number of iterations is 20,000, with early stopping if the training loss or testing loss does not decrease for 1000 iterations. For fine-tuning, we use the same optimization procedure (ADAM followed by L-BFGS-B), but with a smaller dataset $N_r = N_{dat} = 5,000$, a smaller maximum iteration of 5000 steps, and a smaller initial learning rate of 0.0001.

In Fig. A.11, we show an example of the training loss for patient P5 with **FET+SEG**. The left figure shows the training

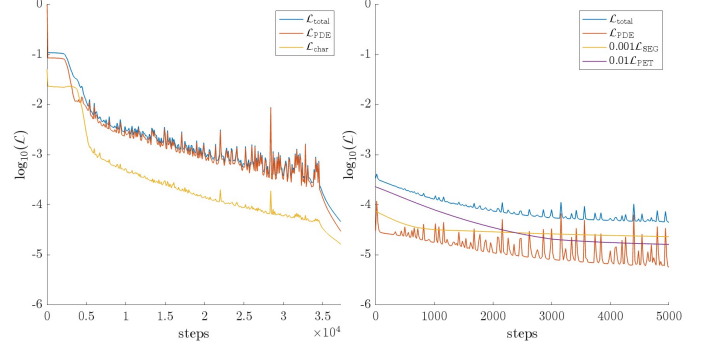


Fig. A.11: Example of training loss for patient P5 with **FET+SEG**. The left figure shows the training loss for pre-training with residual loss and u^{FDM} . The right figure shows the training loss for fine-tuning with segmentation loss and PET loss. The weights are chosen such that the two loss magnitudes are similar.

loss for pre-training with residual loss and u^{FDM} . The right figure shows the training loss for fine-tuning with segmentation loss and PET loss. The \mathcal{L}_{SEG} is weighted by 0.001 and \mathcal{L}_{FET} (if necessary) is weighted by 0.01, while all the other losses are weighted by 1. These weights are chosen such that the magnitude of the losses are comparable, and are constant throughout the training. While we experimented with some adaptive weighting schemes, which balance different loss terms according to coefficients of variation (Groenendijk et al., 2020), by the norm of the gradients (Chen et al., 2018; Wang et al., 2021), or the standard deviation of the gradients (Maddu et al., 2022), using the fixed weights listed above achieved the best results across all synthetic and patient datasets, without significantly increasing the training time.

Appendix B. Distribution of collocation points

We explain how we sample the collocation points for the residual loss, which affects the training efficiency and accuracy. In Lu et al. (2021b), an adaptive residual refinement technique is used to adaptively increase the density of collocation points in the region where the residual is large. In Wang et al. (2022a), the residuals at early times are adaptively given higher weights. We adopt a similar approach in our work here. We know that the solution of the PDE will have larger gradients at early times, and the solution will be concentrated at the center of the tumor.

The distribution of the collocation points is illustrated in Fig. B.12. Let \mathbf{x}_0 be the centroid of y^{T1Gd} , choose the radius

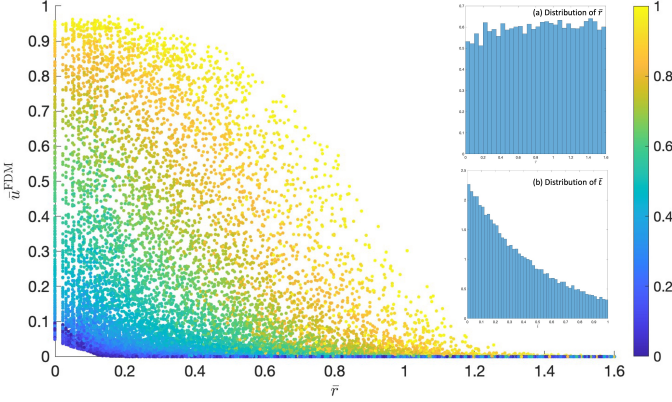


Fig. B.12: The distribution of collocation points for the residual loss in the radial direction is shown as a scatter plot with \bar{u}^{FDM} and r (radii of \mathbf{x}^r) and color-coded by time spanning from 0 to 1. The PDE solution is concentrated at the center where there is a larger gradient at early times, and the collocation points are densely sampled at the center and at early times. Inset (a) shows a histogram of r (normalized to a probability density function), highlighting that due to near-uniform distribution in polar coordinates, \mathbf{x}^r is denser at the center. Inset (b) shows a histogram of time (normalized as a probability density function), indicating a denser sampling in the earlier time periods.

R such that the spherical ball B with center \mathbf{x}_0 and radius R encloses the region where $\bar{u}^{FDM} > 0.001$. Next, we sample the grid points \mathbf{x}_i in C such that \mathbf{x}_i are dense in the center, sparse near the boundary, and t_i are dense at early times and sparse at late times, because the solution u has larger gradients in the tumor center and at early times. More specifically, t_i is sampled from a truncated exponential probability density function $\lambda e^{-\lambda t}$, with $\lambda = 0.5$ and $t \in [0, 1]$. Each spatial coordinate \mathbf{x}_i is resampled with weight $1/(r_i^2)$ in 3d, where r_i is the distance from \mathbf{x}_i to the tumor center \mathbf{x}_0 . We experimented with other static distributions of the collocation points, including uniformly sampling the temporal and spatial coordinates, or densely sampling the spatial coordinates at the transition region between white and gray matter (where the diffusion coefficient changes sharply), and an adaptive residual refinement technique following (Lu et al., 2021b), which recruits the 100 testing points with the largest residual loss into the training points every 1000 iterations, but we did not find significant improvement in accuracy.

Appendix C. Additional results using synthetic data

For all the synthetic data S1-S8, after we obtain the ground truth cell density u^{FDM} by solving the Fisher-KPP PDE using the FDM, we generate spatially correlated noise v by sampling from a Gaussian distribution (mean 0 and standard deviation 2)

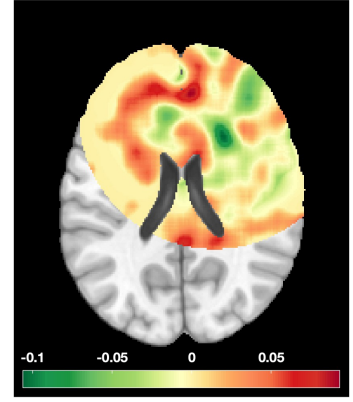


Fig. C.13: Illustration of spatially correlated noise, as employed in Fig. 5. Noise is produced by sampling from a Gaussian distribution (mean 0 and standard deviation 2) at each pixel and subsequently applying a Gaussian filter of size 13.

at each pixel and subsequently apply a Gaussian filter of size 13, as shown in Fig. C.13. We add v to u and threshold the result in $[0, 1]$. The synthetic segmentation and FET signal are generated based on this noisy cell density.

In Table C.2, we show the estimated parameters for the synthetic dataset S1-S8, comparing the results using **FET+SEG** and **SEG** data with the ground truth parameters. In Supplementary Materials, we show all S1-S8 results as in Fig. 3.

Appendix D. Additional results for patient tumors

In Fig. D.14, as supplement to Fig. 5, we compare u^{FDM} and u^{PINN} for patient P5 using **SEG** data. Similar to the results in the synthetic case (Fig. 3), the predicted segmentations of u^{PINN} align more closely with the actual segmentations than u^{FDM} does, while the 1% contour and the predicted density is noisier than that from u^{FDM} . This suggests that when the model cannot fully account for the data, the PINN reduces the overall cost by reducing the data loss at the expense of the PDE loss. Accordingly, the u^{PINN} metrics, including DICE scores and correlations with FET signal, tend to be better than u^{FDM} metrics (see Appendix D, Table D.3). This might not be desired in terms of PDE-constrained optimization, as the constraint (e.g., the PDE) is not satisfied. However, in a data-driven approach, the PDE loss can be considered as a regularization term that prevents overfitting (Balcerak et al., 2023).

We show the results for patients P1-P8 using **FET+SEG**

case	μ_D	μ_R	x_0	y_0	z_0	u_c^{FLAIR}	u_c^{T1Gd}	m	A
S1 (GT)	0.796	0.919	164	116	99	0.35	0.6	1	0.1
S1 (PET+SEG)	0.785	0.91	165	115	98.1	0.357	0.617	0.944	0.084
S1 (SEG)	0.8	0.922	165	115	98.1	0.385	0.639	-	-
S2 (GT)	0.796	0.919	65	70	99	0.35	0.6	1	0.1
S2 (PET+SEG)	0.766	0.91	64.1	70	99.1	0.381	0.635	0.97	0.112
S2 (SEG)	0.77	0.916	64.1	70	99.1	0.399	0.649	-	-
S3 (GT)	0.796	0.943	164	116	99	0.3	0.6	1	0.1
S3 (PET+SEG)	0.916	0.962	164	118	100	0.359	0.628	1.01	0.136
S3 (SEG)	0.92	0.964	164	118	100	0.393	0.654	-	-
S4 (GT)	1.02	0.935	65	70	99	0.3	0.6	1	0.1
S4 (PET+SEG)	0.908	0.959	64	68	99	0.321	0.665	0.857	0.0658
S4 (SEG)	0.911	0.963	64	68	99	0.332	0.678	-	-
S5 (GT)	0.887	0.938	164	116	99	0.3	0.7	1	0.1
S5 (PET+SEG)	0.889	0.953	166	116	100	0.3	0.7	0.961	0.0736
S5 (SEG)	0.892	0.953	166	116	100	0.31	0.7	-	-
S6 (GT)	0.849	0.98	65	70	99	0.3	0.7	1	0.1
S6 (PET+SEG)	0.888	0.956	63	68	99	0.3	0.673	0.999	0.0697
S6 (SEG)	0.888	0.957	63	68	99	0.3	0.672	-	-
S7 (GT)	0.756	0.962	65	70	99	0.3	0.65	1	0.1
S7 (PET+SEG)	0.901	0.96	64	69	98	0.328	0.647	1.01	0.113
S7 (SEG)	0.906	0.961	64	69	98	0.344	0.657	-	-
S8 (GT)	0.756	0.962	164	116	99	0.3	0.65	1	0.1
S8 (PET+SEG)	0.924	0.971	165	115	99	0.331	0.656	1.02	0.117
S8 (SEG)	0.929	0.973	165	115	99	0.353	0.669	-	-

Table C.2: Estimated parameters from the synthetic dataset using **SEG** and **FET+SEG**, compared with ground truth (GT) values.

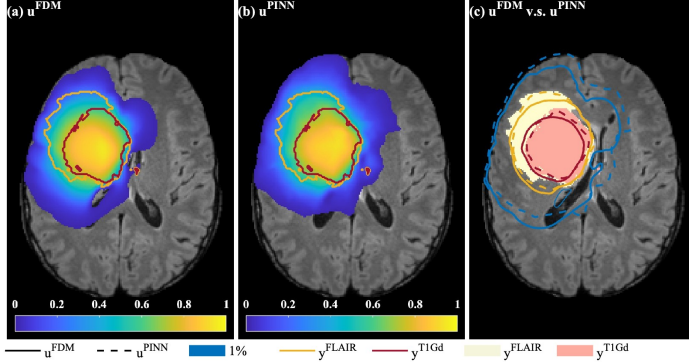


Fig. D.14: Comparison of predicted tumor cell densities u^{FDM} and u^{PINN} for patient P5 using **SEG** data, as supplement to Fig. 5. u^{PINN} is influenced by the noise.

	DICE ^{T1Gd}	DICE ^{FLAIR}	corr ^{FET}
SEG	0.747(± 0.089)	0.678(± 0.162)	0.421(± 0.231)
SEG+FET	0.753(± 0.084)	0.690(± 0.165)	0.473(± 0.217)

Table D.3: Average and standard deviation of DICE scores and correlation with FET signals for all 24 patients using u^{PINN} . The metrics are in general better than those using u^{FDM} (in Table 1) because u^{PINN} might sacrifice fidelity to the PDE to fit the data.

data in Fig.D.15. In Table D.4, the estimated parameters P1-P8 are shown, using both **SEG** and **FET+SEG** data, and these are compared with the results from Lipková et al. (2019). We

also compute various metrics to evaluate the performance of the methods, including DICE scores for both FLAIR and T1Gd segmentations, denoted as $DICE^{FLAIR}$ and $DICE^{T1Gd}$, as well as correlations with FET signals, denoted as $corr^{FET}$. For results using **FET+SEG** data, $corr^{FET}$ is the correlation between the predicted FET signal and the predicted FET (Eq (9)). For results using **SEG** data, which does not consider the imaging model for FET signal, $corr^{FET}$ is the correlation between the predicted FET signal and the predicted cell density. Note that the imaging model of FET in Lipková et al. (2019) does not include the intercept A in Eq. (9).

We compare the outcomes using **FET+SEG** data and using **SEG** alone. It is observed that the estimated parameters and metrics are quite similar; however, incorporating the PET data loss appears to slightly enhance the correlation with the FET signal, at the expense of a marginally lower DICE score for the segmentations.

We also compare the parameters estimated from Lipková et al. (2019) with those obtained through our method. For

parameters in Lipková et al. (2019), the MAP estimate of $(D, \rho, t_{\text{end}})$ is used to compute D/ρ and the non-dimensional \mathcal{D} and \mathcal{R} based on our estimated \mathcal{D} and \mathcal{R} . We can see that \mathcal{R} are similar, whereas there is a larger discrepancy in \mathcal{D} values for P2, P3, P5, and P7. The D/ρ ratio exhibits a larger discrepancy for P2 and P3. In terms of the metrics, the performance is similar. The observed differences could be ascribed to the Bayesian methods' capability to explore a larger parameter space, whereas our training process tends to find parameters close to the initial guess. Despite the variation in parameters, the DICE score and correlation with the FET signal remain similar. In Lipková et al. (2019), the DICE score of T1Gd segmentation is 0, potentially due to a different definition of y^{T1Gd} : in their method, it only comprises the enhancing region, while ours additionally includes the necrotic core. Given there is little T1Gd enhancement for this patient, the majority of the inference is dictated by their model's attempt to fit the fact that cell density below the cut-off is not discernible outside of the T1Gd-enhancing region, resulting in a high u_c^{T1Gd} .

In Table D.5, we show the metrics for predictions using the characteristic parameters, that is, based on \bar{u}^{FDM} . For all cases, $\mu_{\mathcal{D}} = \mu_{\mathcal{R}} = 1$, $m = 1$, $A = 0$, $u_c^{\text{T1Gd}} = 0.6$, $u_c^{\text{FLAIR}} = 0.35$. The morphologies of these patient-specific characteristic tumors are shown in Fig. D.16. Thus, although it is very efficient to generate the characteristic tumors, without fine-tuning, the performance is not as good as the results with fine-tuning (compare with Table. D.4 and Fig. 7)

Figure 8 shows that the personalized CTV from either **FET+SEG** or **SEG**, with an efficiency of 66% and volume of 73 mm^3 , is less efficient and smaller compared to the RTOG CTV, which has an efficiency of 88% and a volume of 178 mm^3 . We investigate this further in Fig. D.21, where we show the sagittal view of (A) the pre-operative tumor and (B) the recurrent tumor. The prediction based on pre-operative tumor is good, with $\text{DICE}^{\text{T1Gd}} 0.76$ and $\text{DICE}^{\text{FLAIR}} 0.69$. Both the recurrent tumor core and the edema regions are larger than the corresponding pre-operative regions. Quantitatively, the percentage of CTV that covers the recurrent tumor core is 44% for RTOG

CTV and 63% for the personalized CTV from **FET+SEG**, which suggests that the personalized CTV is capturing the infiltration pathway, as it spares more normal tissue than RTOG CTV.

Several factors may contribute to the notably large size of the recurrent tumor. Firstly, since the post-operative tumor core region is also larger than the pre-operative tumor core region, it is possible that the resection was not complete, and the residual tumor cell keeps growing. Secondly, acute reactive changes after surgery or radiation can disrupt the fluid regulation in the brain, leading to edema (Ohmura et al., 2023). While our study assumes the edema region as part of the tumor, indicating tumor infiltration (Ohmura et al., 2023), the differentiation between peritumoral edema and glioma invasion remain a significant challenge and is an active area of research (Ohmura et al., 2023).

Appendix E. Estimation of characteristic parameters

We ignore the geometry of the brain and consider a spherically symmetric geometry: a homogenous sphere of radius R sufficiently larger than the brain (here we use $R = 180$). Taking $\mu_{\mathcal{D}} = 1$, $\mu_{\mathcal{R}} = 1$, and $P(\mathbf{x}) = 1$ then the PDE (2) reduces to the radially symmetric system $u(r, t)$, where $r \in [0, R]$, $t \in [0, 1]$,

$$\begin{cases} \frac{\partial u}{\partial t} = \mathcal{D} \frac{1}{r^2} \frac{\partial}{\partial r} \left(r^2 \frac{\partial}{\partial r} u \right) + \mathcal{R} u (1 - u) \\ \frac{\partial u}{\partial r} = 0 \quad \text{on } r = 0 \quad \text{and } r = R \\ u = 0.1 \exp(-0.1r) \quad \text{at } t = 0 \end{cases} \quad (\text{E.1})$$

The detailed procedure for estimating the characteristic parameters is as follows:

- Compute the centroid of the FLAIR segmentation y^{FLAIR} , denoted as \mathbf{x}_0 , which is used as the initial guess for the tumor center.
- Find the radius $R_{\text{seg}}^{\text{FLAIR}}$ such that the sphere with center \mathbf{x}_0 and radius $R_{\text{seg}}^{\text{FLAIR}}$ encloses the FLAIR segmentation y^{FLAIR} :

$$R_{\text{seg}}^{\text{FLAIR}} = \max\{r | r = \|\mathbf{x} - \mathbf{x}_0\|, y^{\text{FLAIR}}(\mathbf{x}) = 1\}$$

Similarly find the radius $R_{\text{seg}}^{\text{T1Gd}}$ for y^{T1Gd} .

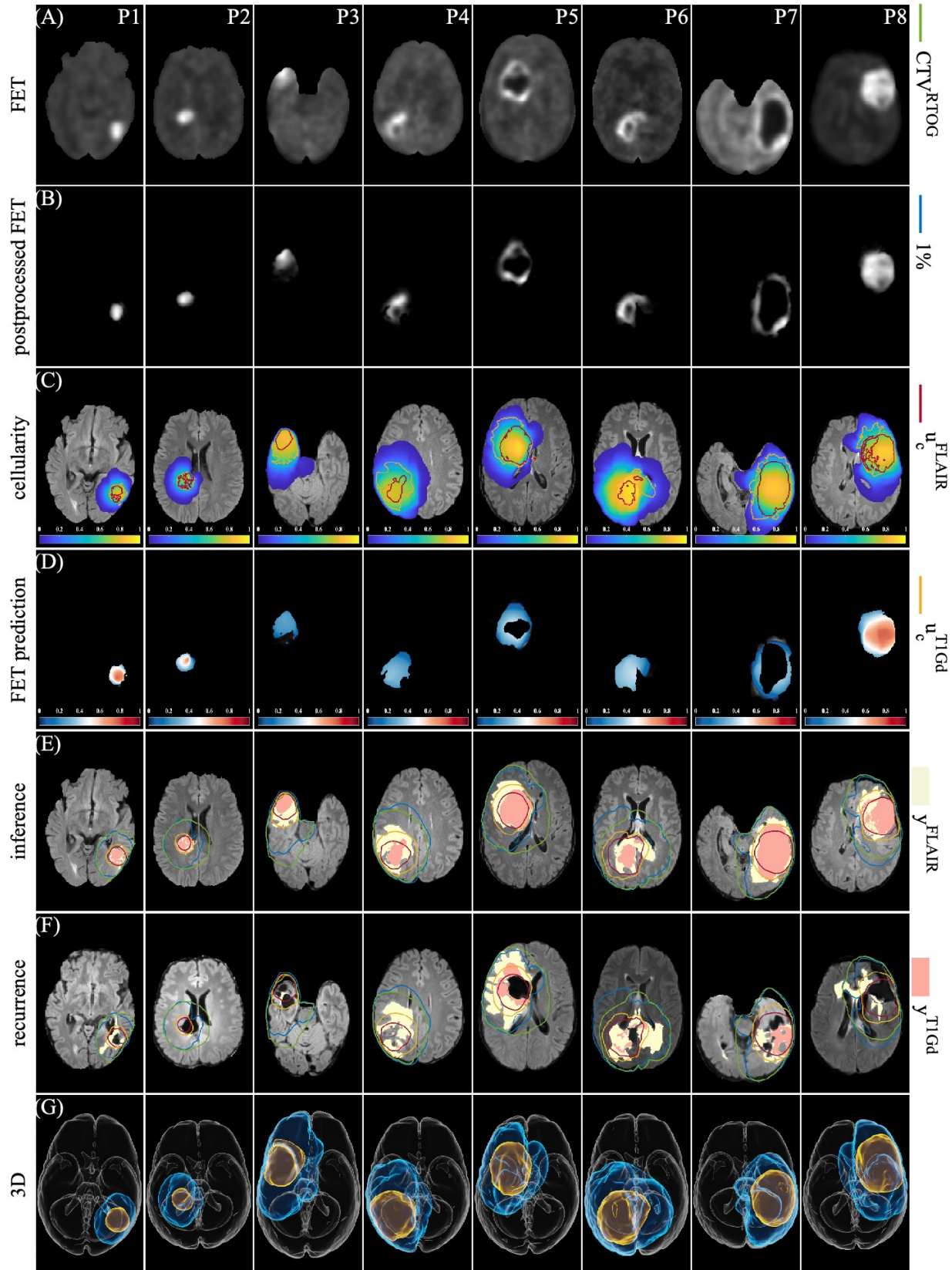


Fig. D.15: Parameter Estimation Results for Patients P1-P8 using **FET+SEG**. Pre-operative T1Gd and FLAIR are identical to Fig. 7. (A) FET signal. (B) Pre-processed PET by subtracting the background average and normalized to [0, 1]. (C) Superimposition of predicted tumor cell density u_c^{FDM} on actual segmentations: T1Gd (yellow line) and FLAIR (red line). (D) Predicted FET signal. (E) Overlap of inferred segmentations: u_c^{FLAIR} (yellow line) and u_c^{T1Gd} (red line) on actual segmentations: T1Gd (beige fill) and FLAIR (pink fill); Margins for CTV^{RTOG} (green) and CTV^P (blue). (F) Tumor recurrence, compared with margins for CTV^{RTOG} (green) and CTV^P (blue). (G) 3D reconstructions of CTV^P and u_c^{FLAIR} isosurfaces.

case	μ_D	μ_R	D/ρ	u_c^{FLAIR}	u_c^{T1Gd}	m	A	$DICE^{\text{FLAIR}}$	$DICE^{\text{T1Gd}}$	$corr_{\text{FET}}$
P1 (*)	0.83	0.896	6.48	0.521	0.693	1.04	-	0.723	0.661	0.777
P1 (SEG)	0.899	0.899	8	0.5	0.603	-	-	0.702	0.69	0.71
P1 (SEG+PET)	0.887	0.894	7.93	0.396	0.512	1.18	0.219	0.619	0.562	0.713
P2 (*)	0.313	0.894	2.5	0.436	0.559	1.18	-	0.747	0.651	0.844
P2 (SEG)	0.814	0.877	7.43	0.493	0.611	-	-	0.726	0.537	0.817
P2 (SEG+PET)	0.802	0.859	7.47	0.4	0.532	1.2	0.261	0.762	0.639	0.829
P3 (*)	1.77	0.943	84.6	0.347	0.614	1.08	-	0.511	0.554	0.475
P3 (SEG)	0.764	0.825	37	0.5	0.7	-	-	0.553	0.801	0.505
P3 (SEG+PET)	0.763	0.821	37.2	0.5	0.7	0.8	0.394	0.551	0.805	0.54
P4 (*)	0.822	0.83	22.3	0.416	0.796	0.989	-	0.426	0	0.591
P4 (SEG)	0.844	0.948	24.9	0.49	0.7	-	-	0.709	0.659	0.478
P4 (SEG+PET)	0.842	0.94	25.1	0.435	0.658	0.874	0.34	0.715	0.592	0.49
P5 (*)	1.31	0.86	22.9	0.374	0.601	0.98	-	0.813	0.802	0.503
P5 (SEG)	0.905	0.933	15.5	0.415	0.7	-	-	0.808	0.803	0.401
P5 (SEG+PET)	0.898	0.901	15.9	0.331	0.607	0.8	0.249	0.81	0.789	0.406
P6 (*)	0.819	0.972	15.2	0.369	0.614	1.07	-	0.503	0.242	0.513
P6 (SEG)	0.924	0.943	21.6	0.5	0.7	-	-	0.578	0.362	0.502
P6 (SEG+PET)	0.924	0.937	21.7	0.5	0.7	0.8	0.342	0.585	0.376	0.532
P7 (*)	1.3	0.93	28	0.362	0.604	1.19	-	0.775	0.747	0.423
P7 (SEG)	0.848	0.942	25.2	0.466	0.7	-	-	0.8	0.779	0.438
P7 (SEG+PET)	0.843	0.915	25.8	0.419	0.628	0.8	0.28	0.791	0.788	0.429
P8 (*)	0.978	0.909	19.4	0.355	0.602	1.15	-	0.755	0.69	0.74
P8 (SEG)	0.927	0.954	25.3	0.5	0.683	-	-	0.746	0.694	0.624
P8 (SEG+PET)	0.919	0.952	25.1	0.401	0.61	1.2	0.289	0.741	0.653	0.627

Table D.4: Parameters estimated for Patients P1-P8 using **FET+SEG** and **SEG** data, compared with results from Lipková et al. (2019)(*). Parameters that are not included in the model are marked with “-”. Metrics include DICE score for both FLAIR and T1Gd segmentations, as well as correlation with the FET signal (see Appendix D).

case	$DICE^{\text{FLAIR}}$	$DICE^{\text{T1Gd}}$	$corr_{\text{FET}}$
P1 (char)	0.409	0.397	0.658
P2 (char)	0.399	0.436	0.759
P3 (char)	0.478	0.293	0.402
P4 (char)	0.568	0.259	0.446
P5 (char)	0.74	0.565	0.389
P6 (char)	0.409	0.188	0.469
P7 (char)	0.727	0.687	0.429
P8 (char)	0.635	0.514	0.611

Table D.5: Metrics for results using the characteristic parameters without fine-tuning. For all cases, $\mu_D = \mu_R = 1$, $m = 1$, $A = 0$, $u_c^{\text{T1Gd}} = 0.6$, $u_c^{\text{FLAIR}} = 0.35$. Without fine-tuning, the metrics are not as good as the results in Table D.4.

- For $\bar{D}/\bar{\rho} = 0.1 : 0.1 : 1$ (matlab notation) and $L = 10 : 5 : 90$, solve (E.1). Based on Lipková et al. (2019), we assume $u_c^{\text{FLAIR}} = 0.35$ and $u_c^{\text{T1Gd}} = 0.6$. Record the radii corresponding to u_c^{FLAIR} and u_c^{T1Gd} as $R_{\text{sph}}^{\text{FLAIR}}$ and $R_{\text{sph}}^{\text{T1Gd}}$
- find the combination $\bar{D}/\bar{\rho}$ and L such that sum of the relative error $|R_{\text{seg}}^{\text{FLAIR}} - R_{\text{sph}}^{\text{FLAIR}}|/R_{\text{seg}}^{\text{FLAIR}} + |R_{\text{seg}}^{\text{T1Gd}} - R_{\text{sph}}^{\text{T1Gd}}|/R_{\text{seg}}^{\text{T1Gd}}$ is minimized.
- This yields the patient specific characteristic parameters $\bar{D}/\bar{\rho}$, L . We solve the PDE in the brain geometry with

$\mu_D = \mu_R = 1$ to obtain the characteristic solution \bar{u}^{FDM} .

We show the characteristic parameters in Table E.7 (synthetic cases S1-S8), Table E.8 (patients P1-P8), and Table E.9 (patients Q1-Q16).

Appendix F. Effect of different types of data loss

We perform a series of experiments using synthetic data S1-S8 to study the effect of different types of data in the fine-tuning stage. As in Section 2.3, let $u(\mathbf{x}, t)$ be the function represented

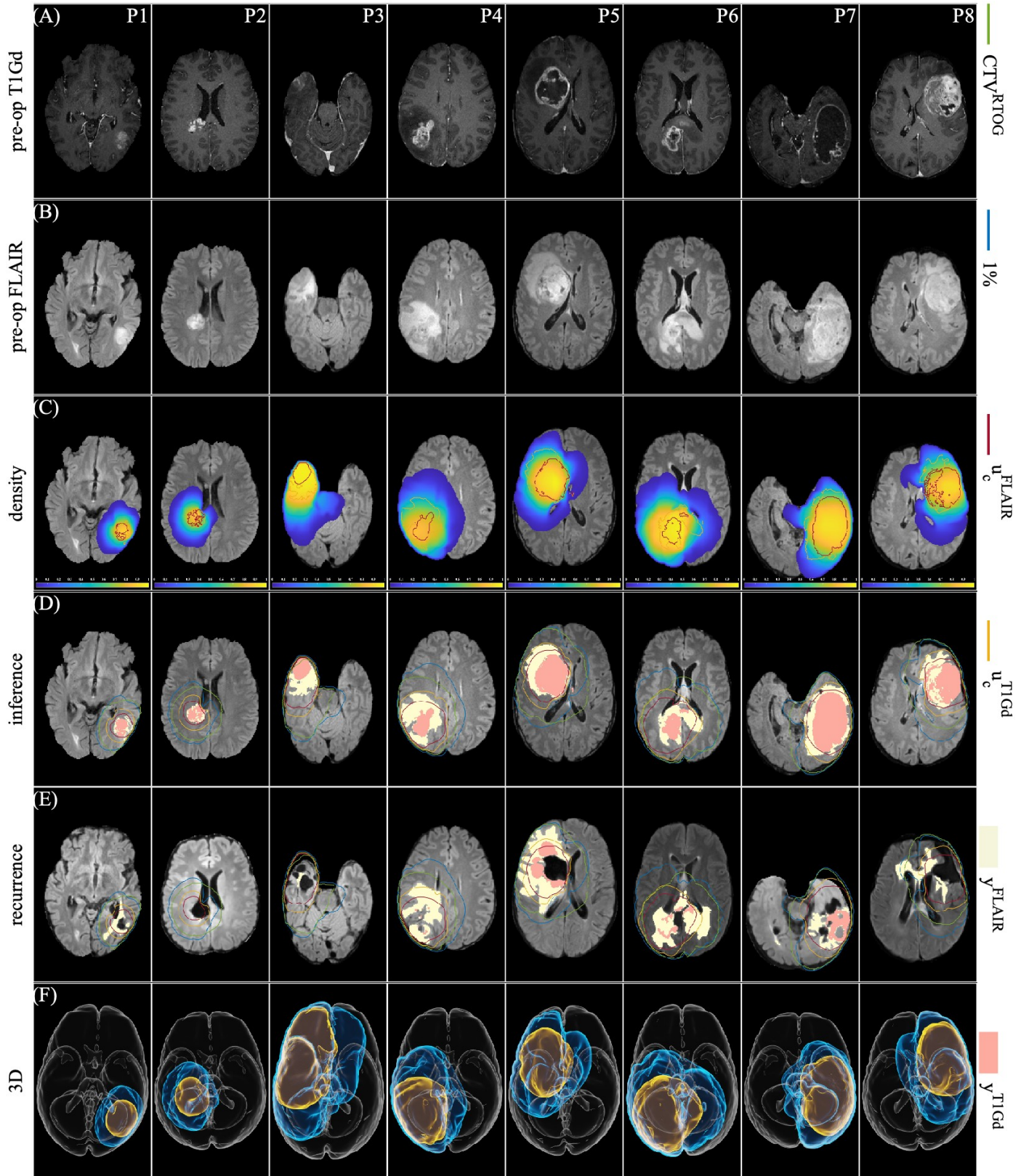


Fig. D.16: Results for Patients P1-P8 using characteristic parameters without fine-tuning. For all cases, $\mu_D = \mu_R = 1$, $m = 1$, $A = 0$, $u_c^{\text{T1Gd}} = 0.6$, $u_c^{\text{FLAIR}} = 0.35$. (a) Pre-operative T1Gd. (b) Pre-operative FLAIR. (c) Superimposition of predicted tumor cell density u_c^{FDM} on actual segmentations: T1Gd (yellow line) and FLAIR (red line). (d) Predicted FET signal. (d) Overlap of inferred segmentations: u_c^{FLAIR} (yellow line) and u_c^{T1Gd} (red line) on actual segmentations: T1Gd (beige fill) and FLAIR (pink fill); Margins for CTV^{RTOG} (green) and CTV^P (glue, 1% contour of u_c^{FDM}). (e) Tumor recurrence, compared with margins for CTV^{RTOG} (green) and CTV^P (blue). (f) 3D reconstructions of CTV^P and u_c^{FLAIR} isosurfaces.

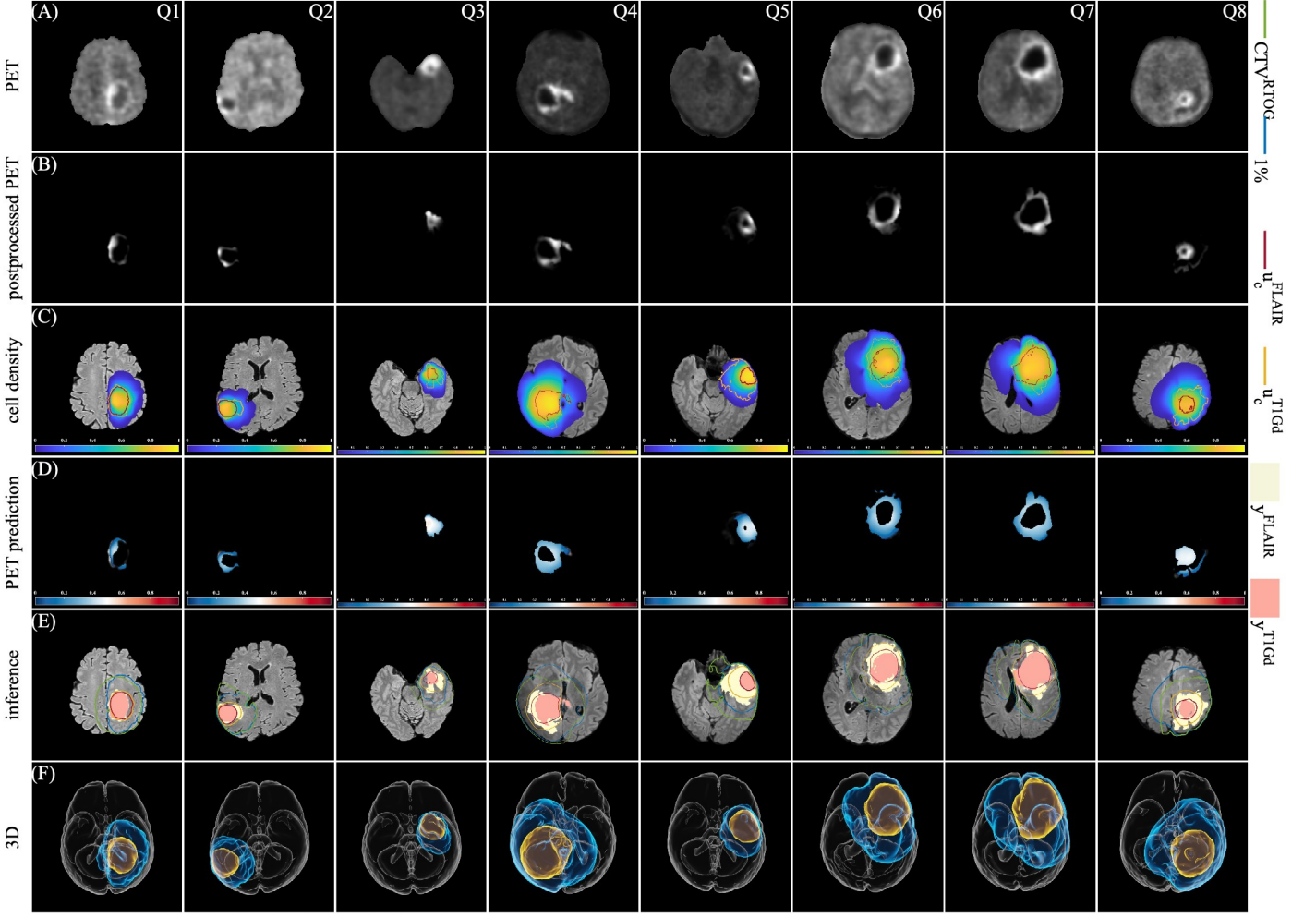


Fig. D.17: Parameter Estimation Results for Patients Q1-Q8 using **FET+SEG**. Results with **SEG** is shown in Fig. D.17.

by the PINN. For the synthetic dataset, we have the ground truth cell density u^{GT} . Unlike the main text, here we do not perturb the u^{GT} with noise. As in Eq.(19), the total loss for fine-tuning has three components: residual loss \mathcal{L}_{PDE} , data loss \mathcal{L}_{data} , and regularization loss \mathcal{L}_β for the parameters $\beta \in \Theta$:

$$\mathcal{L}_{total} = \mathcal{L}_{PDE} + \mathcal{L}_{data} + \sum_{\beta \in \Theta} \mathcal{L}_\beta, \quad (F.1)$$

where \mathcal{L}_{data} depends on the type of data used for fine-tuning. We have studied the results using **FET+SEG** or **SEG** only data, and we consider two additional types of data and their corresponding data loss functions:

- ground truth cell density at residual collocation points (time goes from $[0,1]$), denoted as **u-t-all** in Table F.10.

$$\mathcal{L}_{data} = \frac{1}{N_r} \sum_{i=1}^{N_r} \left(\phi(\mathbf{x}_i^r) u(\mathbf{x}_i^r, t_i) - \phi(\mathbf{x}_i^r) u^{GT}(\mathbf{x}_i^r, t_i) \right)^2.$$

- ground truth cell density at data collocation points (at time 1), denoted as **u-t-end** in Table F.10.

$$\mathcal{L}_{data} = \frac{1}{N_{dat}} \sum_{i=1}^{N_{dat}} \left(\phi(\mathbf{x}_i^{dat}) u(\mathbf{x}_i^{dat}, 1) - \phi(\mathbf{x}_i^{dat}) u^{GT}(\mathbf{x}_i^{dat}, 1) \right)^2.$$

These two cases do not involve the imaging model, and the trainable parameters are $\{\mu_{\mathcal{D}}, \mu_{\mathcal{R}}, \mathbf{x}_0\}$.

In Table F.10, we compare the relative error of $\mu_{\mathcal{D}}$ and $\mu_{\mathcal{R}}$, which are the most important parameters for tumor growth prediction. We see that using the cell density data at all times gives the smallest relative error. Using the cell density data at time 1 gives the second smallest relative error. Using the segmentation and FET data gives similar errors as using the segmentation data only, and both have larger errors than using the cell density data. Of course, the cell density data is not available from current imaging technologies.

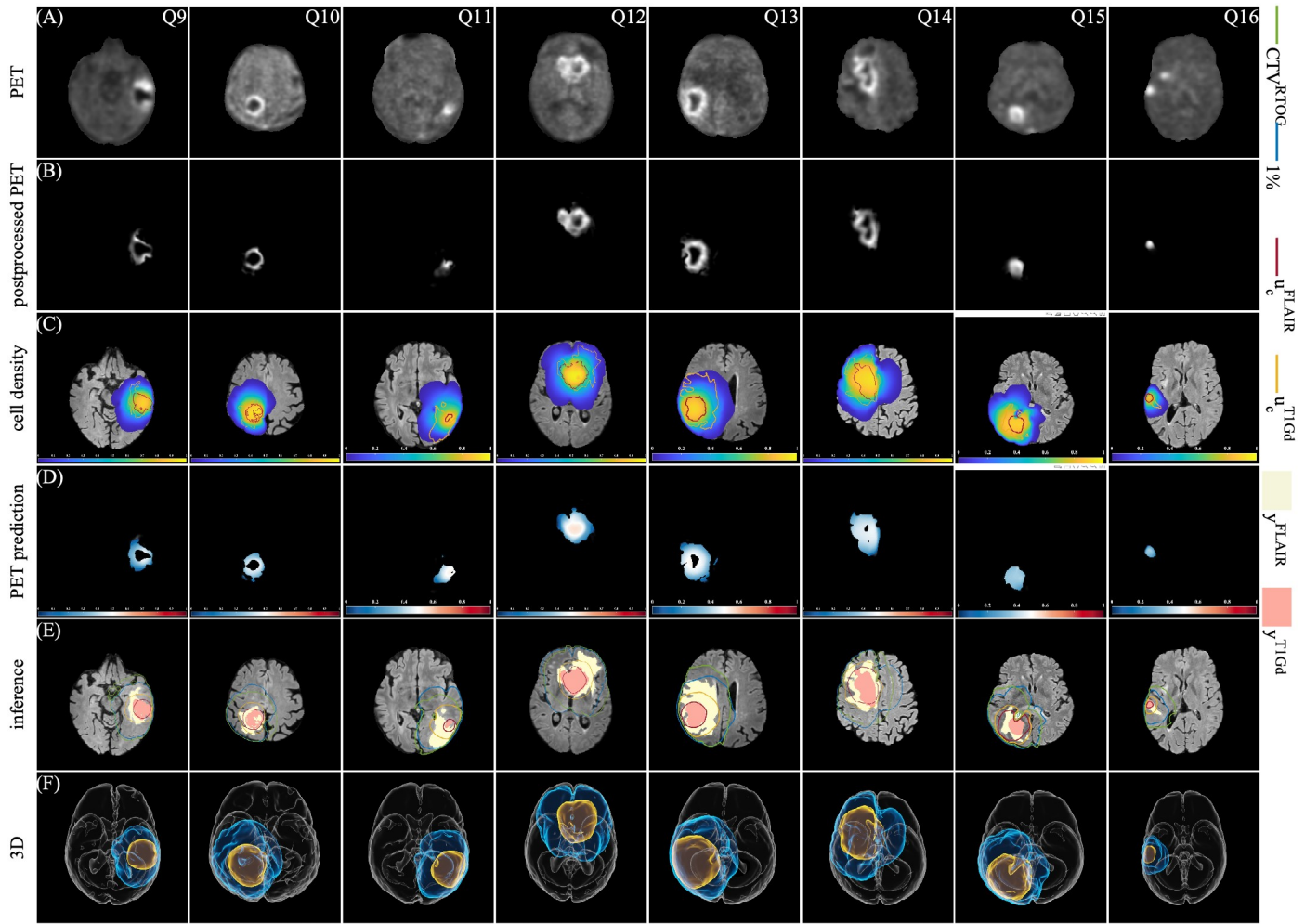


Fig. D.18: Parameter Estimation Results for Patients Q9-Q16 using **FET+SEG**. Results with **SEG** is shown in Fig. D.17.

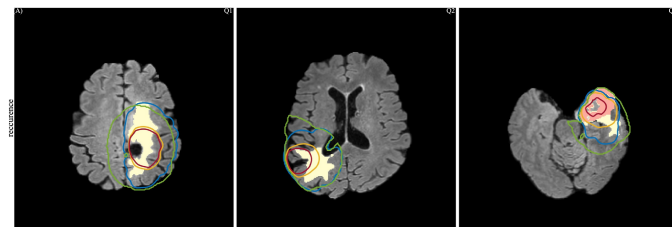


Fig. D.19: Recurrent tumors from patients Q1-Q3 and PDE model predictions using **SEG**, as supplement to Fig. 9.

Appendix G. Correlation of density with FET signals

We observed considerable variability in corr^{FET} , as shown in Table 1. Visually, these signals manifest in distinct patterns: some patients (such as P5, P7 in Fig. D.15) exhibit a ring-like appearance encircling the tumor, while others (P1, P2, P8) display a more uniform, blob-like signal. To quantify the apparent central signal void in some tumors, we calculated the 'solidity'

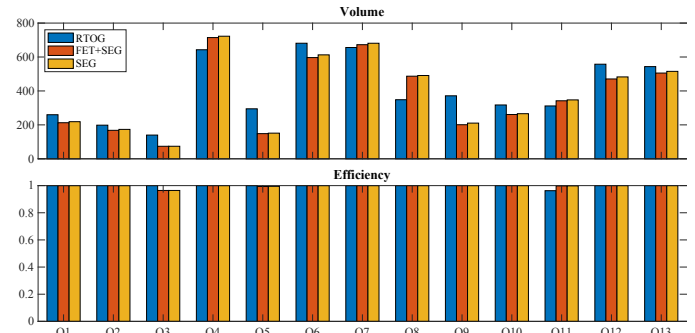


Fig. D.20: Comparison of RTOG CTV (blue) with Personalized CTV (1% isosurface of predicted tumor cell density) from different parameter sources: **FET+SEG** (red), and **SEG** (yellow). (A) Total irradiated volume. (B) Efficiency, as percentage of recurrent tumor core covered by the CTV. Personalized CTV from **FET+SEG**, and **SEG** present reduced or similar irradiation volumes while maintaining efficiency comparable to RTOG CTV.

of the FET region, defined as the ratio of the FET region's area to the area of its convex hull. This metric effectively differentiates between morphologies: ring-like signals yield solidity values significantly lower than 1, indicative of a central void,

case	μ_D	μ_R	u_c^{FLAIR}	u_c^{T1Gd}	m	A	$DICE^{FLAIR}$	$DICE^{T1Gd}$	$corr^{FET}$
Q1(SEG)	0.903	0.946	0.5	0.58	-	-	0.777	0.818	0.0993
Q1(SEG+PET)	0.911	0.926	0.435	0.513	0.75	0.247	0.778	0.82	0.0569
Q2(SEG)	0.926	0.959	0.419	0.634	-	-	0.798	0.818	0.0543
Q2(SEG+PET)	0.934	0.938	0.351	0.544	0.75	0.242	0.804	0.828	0.0458
Q3(SEG)	0.906	0.94	0.3	0.7	-	-	0.755	0.688	0.631
Q3(SEG+PET)	0.908	0.938	0.3	0.7	0.75	0.0917	0.755	0.685	0.634
Q4(SEG)	0.938	0.957	0.5	0.768	-	-	0.712	0.729	0.108
Q4(SEG+PET)	0.94	0.95	0.5	0.747	0.75	0.281	0.721	0.725	0.108
Q5(SEG)	0.927	0.97	0.3	0.8	-	-	0.715	0.847	0.655
Q5(SEG+PET)	0.933	0.957	0.3	0.781	0.75	0.245	0.699	0.848	0.704
Q6(SEG)	0.941	0.967	0.464	0.716	-	-	0.789	0.827	0.356
Q6(SEG+PET)	0.94	0.957	0.403	0.644	0.78	0.22	0.795	0.786	0.357
Q7(SEG)	0.91	0.968	0.5	0.726	-	-	0.7	0.777	0.403
Q7(SEG+PET)	0.909	0.961	0.5	0.696	0.762	0.237	0.706	0.772	0.407
Q8(SEG)	0.925	0.977	0.486	0.745	-	-	0.724	0.774	0.389
Q8(SEG+PET)	0.926	0.971	0.465	0.728	0.782	0.17	0.722	0.754	0.395
Q9(SEG)	0.913	0.958	0.481	0.766	-	-	0.627	0.691	0.484
Q9(SEG+PET)	0.912	0.939	0.404	0.716	0.75	0.193	0.641	0.719	0.479
Q10(SEG)	0.943	0.961	0.5	0.792	-	-	0.714	0.69	0.215
Q10(SEG+PET)	0.943	0.951	0.5	0.75	0.75	0.227	0.722	0.683	0.211
Q11(SEG)	0.953	0.96	0.444	0.8	-	-	0.494	0.256	-0.0703
Q11(SEG+PET)	0.96	0.95	0.35	0.8	0.75	0.147	0.515	0.3	-0.0482
Q12(SEG)	0.93	0.977	0.404	0.753	-	-	0.693	0.74	0.412
Q12(SEG+PET)	0.927	0.964	0.378	0.708	0.773	0.189	0.691	0.746	0.401
Q13(SEG)	0.953	0.968	0.3	0.769	-	-	0.697	0.801	0.562
Q13(SEG+PET)	0.955	0.956	0.3	0.738	0.793	0.194	0.69	0.786	0.57
Q14(SEG)	0.913	0.937	0.493	0.7	-	-	0.768	0.663	0.206
Q14(SEG+PET)	0.921	0.924	0.478	0.7	0.75	0.23	0.767	0.676	0.189
Q15(SEG)	0.912	0.942	0.5	0.7	-	-	0.553	0.336	0.351
Q15(SEG+PET)	0.913	0.937	0.5	0.7	0.78	0.314	0.561	0.347	0.355
Q16(SEG)	0.876	0.908	0.5	0.795	-	-	0.536	0.656	0.65
Q16(SEG+PET)	0.88	0.896	0.484	0.76	0.75	0.248	0.534	0.774	0.678

Table D.6: Estimated parameters and metrics for Patients Q1-Q16, comparison between results using **SEG** and **FET+SEG** data.

case	D	ρ	t_{end}	D/ρ	R_{seg}^{FLAIR}	R_{seg}^{T1Gd}	\bar{L}	$\bar{D}/\bar{\rho}$	\mathcal{D}	\mathcal{R}	R_{sph}^{FLAIR}	R_{sph}^{T1Gd}	μ_D	μ_R
S1	0.13	0.025	300	5.2	17.6	11.2	20	6	0.122	8.16	20	13	0.796	0.919
S2	0.13	0.025	300	5.2	16.4	11.1	20	6	0.122	8.16	20	13	0.796	0.919
S3	0.38	0.025	400	15.2	40	28.4	45	18	0.0943	10.6	42	30	0.796	0.943
S4	0.38	0.025	400	15.2	38.4	27.5	40	14	0.0935	10.7	40	31	1.02	0.935
S5	0.52	0.025	400	20.8	44	26.2	50	22	0.0938	10.7	44	30	0.887	0.938
S6	0.52	0.025	400	20.8	41.7	23.9	50	24	0.098	10.2	39	22	0.849	0.98
S7	0.11	0.01	900	11	29.2	18.1	35	14	0.107	9.35	29	17	0.756	0.962
S8	0.11	0.01	900	11	30.4	20.2	35	14	0.107	9.35	29	17	0.756	0.962

Table E.7: Characteristic parameter estimation from synthetic data. Datasets S1, S3, S5, and S8 use $\mathbf{x}_0 = (164, 116, 99)$ while S2, S4, S6, and S7 use $\mathbf{x}_0 = (65, 70, 99)$. For this synthetic data, the estimated values for μ_D and μ_R are near 1, which is the targeted outcome.

whereas blob-like signals approach a solidity of 1, reflecting a more homogenous signal distribution. Figure G.22 demonstrates a notable positive correlation between $corr^{FET}$ and the solidity of the FET region, indicating that our initial assumption of a linear relationship between cellular density and FET

uptake may not universally apply, particularly in cases exhibiting ring-like signal patterns.

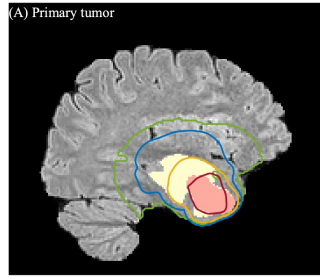
Two factors might contribute to the ring-like FET signals. Firstly, tumor necrosis, a common feature in GBM, results in non-viable, metabolically inactive tissue, which inherently

case	D	ρ	t_{end}	D/ρ	R_{seg}^{FLAIR}	R_{seg}^{T1Gd}	\bar{L}	$\bar{D}/\bar{\rho}$	\mathcal{D}	\mathcal{R}	R_{sph}^{FLAIR}	R_{sph}^{T1Gd}	μ_D	μ_R
P1	0.188	0.029	273	6.48	23.4	16.7	25	8	0.113	8.84	24	16	0.726	0.896
P2	0.06	0.024	338	2.5	24.2	17	25	8	0.113	8.84	24	16	0.286	0.917
P3	0.846	0.01	1090	84.6	77.9	33.8	80	40	0.0791	12.6	75	59	1.83	0.865
P4	0.223	0.01	848	22.3	48.5	23.4	55	28	0.0962	10.4	41	23	0.65	0.816
P5	2.45	0.107	93.3	22.9	44.9	38.1	45	16	0.0889	11.3	46	36	1.27	0.887
P6	0.44	0.029	406	15.2	51.4	42.2	55	22	0.0853	11.7	55	43	0.693	1
P7	0.196	0.007	1580	28	53.2	39.4	60	28	0.0882	11.3	53	38	0.976	0.976
P8	0.484	0.025	392	19.4	45.7	30.3	55	26	0.0927	10.8	46	31	0.676	0.908

Table E.8: Characteristic parameter estimation for Patients P1-P8. Parameters D , ρ , and t_{end} are from Lipková et al. (2019) and used to compute μ_D and μ_R .

case	R_{seg}^{FLAIR}	R_{seg}^{T1Gd}	\bar{L}	$\bar{D}/\bar{\rho}$	\mathcal{D}	\mathcal{R}	R_{sph}^{FLAIR}	R_{sph}^{T1Gd}
Q1	32.5	26	35	12	0.099	10.1	35	25
Q2	30.5	18.5	35	14	0.107	9.35	29	17
Q3	37.3	15.9	40	18	0.106	9.43	30	14
Q4	55.2	45	60	26	0.085	11.8	57	44
Q5	46.9	20.9	50	24	0.098	10.2	39	22
Q6	56.9	34	65	34	0.0897	11.1	52	34
Q7	58.2	37.9	65	32	0.087	11.5	57	40
Q8	40.1	19.5	50	24	0.098	10.2	39	22
Q9	43	24.6	50	24	0.098	10.2	39	22
Q10	34.9	30.4	40	14	0.0935	10.7	40	31
Q11	48.8	13.6	55	30	0.0996	10	36	11
Q12	50.2	34.9	55	24	0.0891	11.2	51	37
Q13	60.2	25.1	65	36	0.0923	10.8	48	27
Q14	49.8	41.2	50	18	0.0849	11.8	52	42
Q15	49.8	34.9	50	20	0.0894	11.2	48	36
Q16	26.2	8.06	30	12	0.115	8.66	23	10

Table E.9: Characteristic parameter estimation for Patients Q1-Q16.

Fig. D.21: Comparison of RTOG CTV (green) with Personalized CTV FET+SEG (blue) for patient Q13 over (A) pre-operative tumor and (B) recurrent tumor. Overlap of inferred segmentations u_c^{FLAIR} (yellow line) and u_c^{T1Gd} (red line) on actual segmentations: T1Gd (beige fill) and FLAIR (pink fill); Margins for CTV^{RTOG} (green) and CTV^P (blue).

shows reduced FET uptake (Meyer et al., 2021; la Fougère et al., 2011). Secondly, the partial volume effect might also play a role that is not captured by our image model (Soret et al., 2007) Since FET-PET spatial resolution is 4 mm, larger than the 1 mm resolution of MRI, signal averaging between active tumor regions and adjacent necrotic or non-tumor areas can lead to an

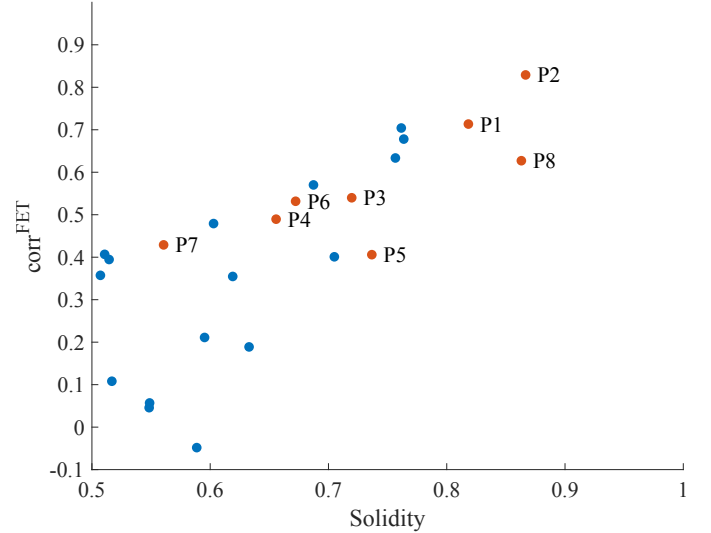


Fig. G.22: Correlation between FET signal and solidity of the FET region. The correlation is 0.757 with p-value 1.8e-5. Ring-like FET signals has solidity values lower than 1, indicative of a central void, and is related to lower correlation between predicted cell densities and FET signals.

underestimation of tracer uptake. These findings suggest that a more nuanced model may be required to accurately interpret

case	μ_D				μ_R			
	u-t-all	u-t-end	FET+SEG	SEG	u-t-all	u-t-end	FET+SEG	SEG
median	5.56	6	7.48	7.58	0.628	2.93	1.35	1.25
mean	5.62	6.92	9.7	9.62	1.09	2.54	1.37	1.45
std	4.74	3.99	8.86	8.45	1.2	1.53	1.07	0.823

Table F.10: Statistics of absolute relative error (%) for μ_D and μ_R in the synthetic dataset (S1-S8) using varied data losses for fine-tuning. **u-t-all** uses the ground truth cell density at residual collocation points over times in [0,1]. Meanwhile, **u-t-end** uses ground truth cell density at data collocation points at time 1. **FET+SEG** uses noisy segmentation and PET data. **SEG** uses noisy segmentation data only.

FET signals, especially in the presence of heterogeneous tumor morphologies. Refining our model to account for these variations presents a promising avenue for future research.

Appendix H. Effect of Personalized characteristic parameters

We use synthetic data to demonstrate the importance of using personalized characteristic parameters for pre-training in our method. We consider an alternative approach that uses the pre-trained network based on S7 (see Table E.7) for fine-tuning. The average length scale \bar{L} and ratio $\bar{D}/\bar{\rho}$ of all synthetic cases are $\bar{L} = 37$ and $\bar{D}/\bar{\rho} = 14.8$, which are close to the values for S7 ($\bar{L} = 35$ and $\bar{D}/\bar{\rho} = 14$). Therefore we can also consider the pre-trained model based on S7 as a pre-trained model with “average” characteristic parameters.

In Table H.11, we compare the relative error of estimated parameters and the performance metrics of two cases: (1) cases S1, S2, S5, S6, which use personalized pre-training, as presented in the main text; and (2) cases S1*, S2*, S5*, S6*, which use the pre-trained network based on S7 for fine-tuning. We see that personalized pre-training recovers the parameters more accurately, and achieves better performance metrics, while using a fixed pre-trained model gives worse results. Note that S2 and S5 also have the same initial location \mathbf{x}_0 as S7, therefore there is no change in the geometry between pre-training and fine-tuning. We believe the suboptimal performance is mainly because the tumors exist different scales (different size and profile, as described by \bar{L} and $\bar{D}/\bar{\rho}$), and the pre-trained model based on S7 can not capture the large variations in the tumor morphology. This leads to challenge in fine-tuning, as the “true” solution might be far from the initial guess, and the training might get stuck in a local minimum. Note that in this investigation, the

pre-trained model is based on one set of characteristic parameters. Pre-training a single network for all patients with different rD , rR and geometry will be a promising future direction.

References

Abadi, M., Agarwal, A., Barham, P., Brevdo, E., Chen, Z., Citro, C., Corrado, G.S., Davis, A., Dean, J., Devin, M., Ghemawat, S., Goodfellow, I., Harp, A., Irving, G., Isard, M., Jia, Y., Jozefowicz, R., Kaiser, L., Kudlur, M., Levenberg, J., Mané, D., Monga, R., Moore, S., Murray, D., Olah, C., Schuster, M., Shlens, J., Steiner, B., Sutskever, I., Talwar, K., Tucker, P., Vanhoucke, V., Vasudevan, V., Viégas, F., Vinyals, O., Warden, P., Wattenberg, M., Wicke, M., Yu, Y., Zheng, X., 2015. TensorFlow: Large-scale machine learning on heterogeneous systems.

Alfonso, J., Talkenberger, K., Seifert, M., Klink, B., Hawkins-Daarud, A., Swanson, K., Hatzikirou, H., Deutsch, A., 2017. The biology and mathematical modelling of glioma invasion: A review. *Journal of the Royal Society Interface* 14. doi:10.1098/rsif.2017.0490.

Balcerak, M., Ezhov, I., Karnakov, P., Litvinov, S., Koumoutsakos, P., Weidner, J., Zhang, R.Z., Lowengrub, J.S., Wiestler, B., Menze, B., 2023. Individualizing Glioma Radiotherapy Planning by Optimization of a Data and Physics Informed Discrete Loss. doi:10.48550/arXiv.2312.05063, arXiv:2312.05063.

Baldock, A., Rockne, R., Boone, A., Neal, M., Bridge, C., Guyman, L., Mргала, M., Rockhill, J., Swanson, K., Trister, A., Hawkins-Daarud, A., Corwin, D., 2013. From Patient-Specific Mathematical Neuro-Oncology to Precision Medicine. *Frontiers in Oncology* 3.

Butner, J., Dogra, P., Chung, C., Pasqualini, R., Arap, W., Lowengrub, J., Cristini, V., Wang, Z., 2022. Mathematical modeling of cancer immunotherapy for personalized clinical translation. *Nature Comput. Sci.* 2, 785–796.

Chaudhuri, A., Pash, G., Hormuth II, D.A., Lorenzo, G., Kapteyn, M., Wu, C., Lima, E.A.B.E., Yankeelov, T.E., Willcox, K., 2023. Predictive Digital Twin for Optimizing Patient-Specific Radiotherapy Regimens under Uncertainty in High-Grade Gliomas. doi:10.48550/arXiv.2308.12429, arXiv:2308.12429.

Chen, Q., Hao, W., 2022. Randomized Newton’s Method for Solving Differential Equations Based on the Neural Network Discretization. *Journal of Scientific Computing* 92, 49. doi:10.1007/s10915-022-01905-9.

Chen, Y., Lu, L., Karniadakis, G.E., Negro, L.D., 2020. Physics-informed neural networks for inverse problems in nano-optics and metamaterials. *Optics Express* 28, 11618–11633. doi:10.1364/OE.384875.

Chen, Z., Badrinarayanan, V., Lee, C.Y., Rabinovich, A., 2018. GradNorm: Gradient Normalization for Adaptive Loss Balancing in Deep Multitask Networks. doi:10.48550/arXiv.1711.02257, arXiv:1711.02257.

Curtin, L., Hawkins-Daarud, A., van der Zee, K.G., Swanson, K.R., Owen, M.R., 2020. Speed Switch in Glioblastoma Growth Rate due to Enhanced Hypoxia-Induced Migration. *Bulletin of Mathematical Biology* 82, 43. doi:10.1007/s11538-020-00718-x.

Desai, S., Mattheakis, M., Joy, H., Protopapas, P., Roberts, S., 2021. One-Shot Transfer Learning of Physics-Informed Neural Networks. <https://arxiv.org/abs/2110.11286v2>.

Ezhov, I., Lipkova, J., Shit, S., Kofler, F., Collomb, N., Lemasson, B., Barbier, E., Menze, B., 2019. Neural Parameters Estimation for Brain Tumor Growth Modeling, in: Shen, D., Liu, T., Peters, T.M., Staib, L.H., Essert, C., Zhou, S., Yap, P.T., Khan, A. (Eds.), *Medical Image Computing and Computer Assisted Intervention – MICCAI 2019*, Springer International Publishing, Cham. pp. 787–795. doi:10.1007/978-3-030-32245-8_87.

Case	μ_D (%)	μ_R (%)	m(%)	A(%)	u_c^{FLAIR} (%)	u_c^{T1Gd} (%)	$\text{DICE}^{\text{FLAIR}}$	$\text{DICE}^{\text{T1Gd}}$	Corr^{FET}
S1	-1.36	-0.90	-5.64	-16.00	2.03	2.79	0.92	0.86	0.98
S1*	163.00	10.60	20.00	49.00	-1.37	-16.70	0.56	0.36	0.91
S2	-3.74	-0.90	-3.03	12.00	8.95	5.77	0.93	0.90	0.98
S2*	191.00	12.40	20.00	238.00	42.80	3.09	0.78	0.66	0.88
S5	0.20	1.55	-3.86	-26.40	0.02	0.00	0.96	0.81	0.98
S5*	-51.00	-12.30	-2.00	-56.40	-0.01	-4.17	0.51	0.38	0.87
S6	4.52	-2.39	-0.13	-30.30	0.00	-3.81	0.94	0.87	0.98
S6*	-48.90	-8.47	-9.69	-59.30	-0.01	2.28	0.60	0.58	0.90

Table H.11: Percentage relative error of estimated parameters and the metrics, comparing effect of personalized pre-training (labeled S[1256]) and fixed pre-training based on pre-trained model using characteristic parameter of S7 (labeled S[1256]*). Personalized characteristic parameters give better results.

Ezhov, I., Mot, T., Shit, S., Lipkova, J., Paetzold, J.C., Kofler, F., Pellegrini, C., Kollovich, M., Navarro, F., Li, H., Metz, M., Wiestler, B., Menze, B., 2022a. Geometry-Aware Neural Solver for Fast Bayesian Calibration of Brain Tumor Models. *IEEE Transactions on Medical Imaging* 41, 1269–1278. doi:10.1109/TMI.2021.3136582.

Ezhov, I., Rosier, M., Zimmer, L., Kofler, F., Shit, S., Paetzold, J.C., Scibilia, K., Steinbauer, F., Maechler, L., Franitzka, K., Amiranashvili, T., Menten, M.J., Metz, M., Conjeti, S., Wiestler, B., Menze, B., 2022b. A for-loop is all you need. For solving the inverse problem in the case of personalized tumor growth modeling, in: *Proceedings of the 2nd Machine Learning for Health Symposium, PMLR*. pp. 566–577.

Ezhov, I., Scibilia, K., Franitzka, K., Steinbauer, F., Shit, S., Zimmer, L., Lipkova, J., Kofler, F., Paetzold, J.C., Canalini, L., Waldmannstetter, D., Menten, M.J., Metz, M., Wiestler, B., Menze, B., 2023. Learn-Morph-Infer: A new way of solving the inverse problem for brain tumor modeling. *Medical Image Analysis* 83, 102672. doi:10.1016/j.media.2022.102672.

Falco, J., Agosti, A., Vetrano, I.G., Bizzì, A., Restelli, F., Broggi, M., Schiavitti, M., DiMeco, F., Ferroli, P., Ciarletta, P., Acerbi, F., 2021. In Silico Mathematical Modelling for Glioblastoma: A Critical Review and a Patient-Specific Case. *Journal of Clinical Medicine* 10, 2169. doi:10.3390/jcm10102169.

Fernandes, C., Costa, A., Osório, L., Lago, R.C., Linhares, P., Carvalho, B., Caeiro, C., 2017. Current Standards of Care in Glioblastoma Therapy, in: De Vleeschouwer, S. (Ed.), *Glioblastoma*. Codon Publications, Brisbane (AU).

Gao, Y., Cheung, K.C., Ng, M.K., 2022. SVD-PINNs: Transfer Learning of Physics-Informed Neural Networks via Singular Value Decomposition. <https://arxiv.org/abs/2211.08760v1>. doi:10.1109/SSCI51031.2022.10022281.

Gholami, A., Mang, A., Biros, G., 2016. An inverse problem formulation for parameter estimation of a reaction–diffusion model of low grade gliomas. *Journal of Mathematical Biology* 72, 409–433. doi:10.1007/s00285-015-0888-x.

Gilbert, M.R., Wang, M., Aldape, K.D., Stupp, R., Hegi, M.E., Jaeckle, K.A., Armstrong, T.S., Wefel, J.S., Won, M., Blumenthal, D.T., Mahajan, A., Schultz, C.J., Erridge, S., Baumert, B., Hopkins, K.I., Tzuk-Shina, T., Brown, P.D., Chakravarti, A., Curran, W.J., Mehta, M.P., 2013. Dose-Dense Temozolomide for Newly Diagnosed Glioblastoma: A Randomized Phase III Clinical Trial. *Journal of Clinical Oncology* 31, 4085–4091. doi:10.1200/JCO.2013.49.6968.

Groenendijk, R., Karaoglu, S., Gevers, T., Mensink, T., 2020. Multi-Loss Weighting with Coefficient of Variations. doi:10.48550/arXiv.2009.01717, [arXiv:2009.01717](https://arxiv.org/abs/2009.01717).

Halperin, E., Bentel, G., Heinz, E., Burger, P., 1989. Radiation therapy treatment planning in supratentorial glioblastoma multiforme: An analysis based on post mortem topographic anatomy with ct correlations. *International Journal of Radiation Oncology, Biology, Physics* 17, 1347–1350. doi:10.1016/0360-3016(89)90548-8.

Hao, W., Hong, Q., Jin, X., Wang, Y., 2023. Gauss Newton method for solving variational problems of PDEs with neural network discretizations. [arXiv:2306.08727](https://arxiv.org/abs/2306.08727).

Harpold, H., Alvord Jr., E., Swanson, K., 2007. The evolution of mathematical modeling of glioma proliferation and invasion. *Journal of Neuropathology and Experimental Neurology* 66, 1–9. doi:10.1097/neu.0b013e31802d9000.

Hoga, C., Biros, G., Abraham, F., Davatzikos, C., 2007. A robust framework for soft tissue simulations with application to modeling brain tumor mass effect in 3D MR images. *Physics in Medicine and Biology* 52, 6893–6908. doi:10.1088/0031-9155/52/23/008.

Hoga, C., Davatzikos, C., Biros, G., 2008. An image-driven parameter estimation problem for a reaction–diffusion glioma growth model with mass effects. *Journal of Mathematical Biology* 56, 793–825. doi:10.1007/s00285-007-0139-x.

Huang, Y., Hao, W., Lin, G., 2022. HomPINNs: Homotopy physics-informed neural networks for learning multiple solutions of nonlinear elliptic differential equations. *Computers & Mathematics with Applications* 121, 62–73. doi:10.1016/j.camwa.2022.07.002.

Hutterer, M., Nowosielski, M., Putzer, D., Jansen, N., Seiz, M., Schocke, M., McCoy, M., Göbel, G., La Fougère, C., Virgolini, I., Trinka, E., Jacobs, A., Stockhamer, G., 2013. [18F]-fluoro-ethyl-l-tyrosine PET: A valuable diagnostic tool in neuro-oncology, but not all that glitters is glioma. *Neuro-Oncology* 15, 341–351. doi:10.1093/neuonc/nos300.

Jagtap, A.D., Mao, Z., Adams, N., Karniadakis, G.E., 2022a. Physics-informed neural networks for inverse problems in supersonic flows. *Journal of Computational Physics* 466, 111402. doi:10.1016/j.jcp.2022.111402.

Jagtap, A.D., Mitsotakis, D., Karniadakis, G.E., 2022b. Deep learning of inverse water waves problems using multi-fidelity data: Application to Serre–Green–Naghdi equations. *Ocean Engineering* 248, 110775. doi:10.1016/j.oceaneng.2022.110775.

Jørgensen, A.C.S., Hill, C.S., Sturrock, M., Tang, W., Karamched, S.R., Gorup, D., Lythgoe, M.F., Parrinello, S., Marguerat, S., Shahrezaei, V., 2023. Data-driven spatio-temporal modelling of glioblastoma. *Royal Society Open Science* 10, 221444. doi:10.1098/rsos.221444.

Karnakov, P., Litvinov, S., Koumoutsakos, P., 2022. Optimizing a Discrete Loss (ODIL) to solve forward and inverse problems for partial differential equations using machine learning tools. doi:10.48550/arXiv.2205.04611, [arXiv:2205.04611](https://arxiv.org/abs/2205.04611).

Karniadakis, G.E., Kevrekidis, I.G., Lu, L., Perdikaris, P., Wang, S., Yang, L., 2021. Physics-informed machine learning. *Nature Reviews Physics* 3, 422–440. doi:10.1038/s42254-021-00314-5.

Kim, J., Lee, K., Lee, D., Jin, S.Y., Park, N., 2020. DPM: A Novel Training Method for Physics-Informed Neural Networks in Extrapolation. doi:10.48550/arXiv.2012.02681, [arXiv:2012.02681](https://arxiv.org/abs/2012.02681).

Konukoglu, E., Clatz, O., Bondiau, P.Y., Delingette, H., Ayache, N., 2010a. Extrapolating glioma invasion margin in brain magnetic resonance images: Suggesting new irradiation margins. *Medical Image Analysis* 14, 111–125. doi:10.1016/j.media.2009.11.005.

Konukoglu, E., Clatz, O., Menze, B.H., Stieljes, B., Weber, M.A., Mandonnet, E., Delingette, H., Ayache, N., 2010b. Image Guided Personalization of Reaction–Diffusion Type Tumor Growth Models Using Modified Anisotropic Eikonal Equations. *IEEE Transactions on Medical Imaging* 29, 77–95. doi:10.1109/TMI.2009.2026413.

Krishnapriyan, A.S., Gholami, A., Zhe, S., Kirby, R.M., Mahoney, M.W., 2021. Characterizing possible failure modes in physics-informed neural networks. doi:10.48550/arXiv.2109.01050, [arXiv:2109.01050](https://arxiv.org/abs/2109.01050).

La Fougère, C., Suchorska, B., Bartenstein, P., Kreth, F.W., Tonn, J.C., 2011. Molecular imaging of gliomas with PET: Opportunities and limitations. *Neuro-Oncology* 13, 806–819. doi:10.1093/neuonc/nor054.

Lê, M., Delingette, H., Kalpathy-Cramer, J., Gerstner, E., Batchelor, T., Unkelbach, J., Ayache, N., 2016. MRI based bayesian personalization of a tu-

mor growth model. *IEEE Transactions on Medical Imaging* 35, 2329–2339. doi:10.1109/TMI.2016.2561098.

Lervåg, K.Y., Lowengrub, J., 2015. Analysis of the diffuse-domain method for solving PDEs in complex geometries. *Communications in Mathematical Sciences* 13, 1473–1500. doi:10.4310/CMS.2015.v13.n6.a6, arXiv:1407.7480.

Li, X., LOWENGRUB, J., RÄTZ, A., VOIGT, A., 2009. Solving pdes in complex geometries: A diffused domain approach. *Communications in mathematical sciences* 7, 81–107.

Li, Z., Kovachki, N., Azizzadenesheli, K., Liu, B., Bhattacharya, K., Stuart, A., Anandkumar, A., 2020. Fourier Neural Operator for Parametric Partial Differential Equations. <https://arxiv.org/abs/2010.08895v3>.

Lipková, J., Angelikopoulos, P., Wu, S., Alberts, E., Wiestler, B., Diehl, C., Preibisch, C., Pyka, T., Combs, S.E., Hadjidoukas, P., Van Leemput, K., Koumoutsakos, P., Lowengrub, J., Menze, B., 2019. Personalized Radiotherapy Design for Glioblastoma: Integrating Mathematical Tumor Models, Multimodal Scans, and Bayesian Inference. *IEEE Transactions on Medical Imaging* 38, 1875–1884. doi:10.1109/TMI.2019.2902044.

Lipková, J., Menze, B., Wiestler, B., Koumoutsakos, P., Lowengrub, J.S., 2022. Modelling glioma progression, mass effect and intracranial pressure in patient anatomy. *Journal of the Royal Society Interface* 19, 20210922. doi:10.1098/rsif.2021.0922.

Lorenzo, G., Ahmed, S.R., au2, D.A.H.I., Vaughn, B., Kalpathy-Cramer, J., Solorio, L., Yankeelov, T.E., Gomez, H., 2023. Patient-specific, mechanistic models of tumor growth incorporating artificial intelligence and big data.

Lu, L., Jin, P., Pang, G., Zhang, Z., Karniadakis, G.E., 2021a. Learning nonlinear operators via DeepONet based on the universal approximation theorem of operators. *Nature Machine Intelligence* 3, 218–229. doi:10.1038/s42256-021-00302-5.

Lu, L., Meng, X., Mao, Z., Karniadakis, G.E., 2021b. DeepXDE: A Deep Learning Library for Solving Differential Equations. *SIAM Review* 63, 208–228. doi:10.1137/19M1274067.

Lu, M.J., Hao, W., Hu, B., Li, S., 2023. Bifurcation analysis of a free boundary model of vascular tumor growth with a necrotic core and chemotaxis. *Journal of Mathematical Biology* 86, 19. doi:10.1007/s00285-022-01862-9.

Lu, M.J., Hao, W., Liu, C., Lowengrub, J., Li, S., 2022. Nonlinear simulation of vascular tumor growth with chemotaxis and the control of necrosis. *Journal of Computational Physics* 459, 111153. doi:10.1016/j.jcp.2022.111153.

Macklin, P., McDougall, S., Anderson, A.R.A., Chaplain, M.A.J., Cristini, V., Lowengrub, J., 2009. Multiscale modelling and nonlinear simulation of vascular tumour growth. *Journal of mathematical biology* 58, 765–798. doi:10.1007/s00285-008-0216-9.

Maddu, S., Sturm, D., Müller, C.L., Sbalzarini, I.F., 2022. Inverse Dirichlet weighting enables reliable training of physics informed neural networks. *Machine Learning: Science and Technology* 3, 015026. doi:10.1088/2632-2153/ac3712.

Mang, A., Toma, A., Schuetz, T., Becker, S., Eckey, T., Mohr, C., Petersen, D., Buzug, T., 2012. Biophysical modeling of brain tumor progression: From unconditionally stable explicit time integration to an inverse problem with parabolic PDE constraints for model calibration. *Medical Physics* 39, 4444–4459. doi:10.1118/1.4722749.

Martens, C., Rovai, A., Bonatto, D., Metens, T., Debeir, O., Decaestecker, C., Goldman, S., Van Simaeys, G., 2022. Deep Learning for Reaction-Diffusion Glioma Growth Modeling: Towards a Fully Personalized Model? *Cancers* 14, 2530. doi:10.3390/cancers14102530.

Menze, B.H., Van Leemput, K., Honkela, A., Konukoglu, E., Weber, M.A., Ayache, N., Golland, P., 2011. A Generative Approach for Image-Based Modeling of Tumor Growth. *Information processing in medical imaging : proceedings of the ... conference* 22, 735–747.

Meyer, H.S., Liesche-Starnecker, F., Mustafa, M., Yakushev, I., Wiestler, B., Meyer, B., Gempt, J., 2021. [18F]FET PET Uptake Indicates High Tumor and Low Necrosis Content in Brain Metastasis. *Cancers* 13, 355. doi:10.3390/cancers13020355.

Ohmura, K., Tomita, H., Hara, A., 2023. Peritumoral Edema in Gliomas: A Review of Mechanisms and Management. *Biomedicines* 11, 2731. doi:10.3390/biomedicines11102731.

Pati, S., Sharma, V., Aslam, H., Thakur, S.P., Akbari, H., Mang, A., Subramanian, S., Biros, G., Davatzikos, C., Bakas, S., 2021. Estimating Glioblastoma Biophysical Growth Parameters Using Deep Learning Regression. *BrainLes (Workshop)* 12658, 157–167. doi:10.1007/978-3-030-72084-1_15.

Raissi, M., Perdikaris, P., Karniadakis, G.E., 2019. Physics-informed neural networks: A deep learning framework for solving forward and inverse problems involving nonlinear partial differential equations. *Journal of Computational Physics* 378, 686–707. doi:10.1016/j.jcp.2018.10.045.

Rockne, R., Rockhill, J.K., Mrugala, M., Spence, A.M., Kalet, I., Hendrickson, K., Lai, A., Cloughesy, T., Alvord, E.C., Swanson, K.R., 2010. Predicting the efficacy of radiotherapy in individual glioblastoma patients *in vivo*: A mathematical modeling approach. *Physics in Medicine & Biology* 55, 3271. doi:10.1088/0031-9155/55/12/001.

Rockne, R.C., Hawkins-Daarud, A., Swanson, K.R., Sluka, J.P., Glazier, J.A., Macklin, P., Hormuth, D.A., Jarrett, A.M., Lima, E.A.B.F., Oden, J.T., Biros, G., Yankeelov, T.E., Curtius, K., Bakir, I.A., Wodarz, D., Komarova, N., Aparicio, L., Bordyuh, M., Rabadan, R., Finley, S.D., Enderling, H., Caudell, J., Moros, E.G., Anderson, A.R.A., Gatenby, R.A., Kaznatcheev, A., Jeavons, P., Krishnan, N., Pelesko, J., Wadhwa, R.R., Yoon, N., Nichol, D., Marusyk, A., Hinczewski, M., Scott, J.G., 2019. The 2019 mathematical oncology roadmap. *Physical Biology* 16, 041005. doi:10.1088/1478-3975/ab1a09.

Rockne, R.C., Trister, A.D., Jacobs, J., Hawkins-Daarud, A.J., Neal, M.L., Hendrickson, K., Mrugala, M.M., Rockhill, J.K., Kinahan, P., Krohn, K.A., Swanson, K.R., 2015. A patient-specific computational model of hypoxia-modulated radiation resistance in glioblastoma using 18F-FMISO-PET. *Journal of The Royal Society Interface* 12, 20141174. doi:10.1098/rsif.2014.1174.

Sarabian, M., Babaee, H., Laksari, K., 2022. Physics-Informed Neural Networks for Brain Hemodynamic Predictions Using Medical Imaging. *IEEE Transactions on Medical Imaging* 41, 2285–2303. doi:10.1109/TMI.2022.3161653.

Saut, O., Lagaert, J.B., Colin, T., Fathallah-Shaykh, H.M., 2014. A Multilayer Grow-or-Go Model for GBM: Effects of Invasive Cells and Anti-Angiogenesis on Growth. *Bulletin of Mathematical Biology* 76, 2306–2333. doi:10.1007/s11538-014-0007-y.

Scheufele, K., Subramanian, S., Biros, G., 2021. Fully Automatic Calibration of Tumor-Growth Models Using a Single mpMRI Scan. *IEEE Transactions on Medical Imaging* 40, 193–204. doi:10.1109/TMI.2020.3024264.

Scheufele, K., Subramanian, S., Mang, A., Biros, G., Mehl, M., 2020. Image-Driven Biophysical Tumor Growth Model Calibration. *SIAM Journal on Scientific Computing* 42, B549–B580. doi:10.1137/19M1275280.

Soret, M., Bacharach, S.L., Buvat, I., 2007. Partial-Volume Effect in PET Tumor Imaging. *Journal of Nuclear Medicine* 48, 932–945. doi:10.2967/jnumed.106.035774.

Souhami, L., Seiferheld, W., Brachman, D., Podgorsak, E., Werner-Wasik, M., Lustig, R., Schultz, C., Sause, W., Okunieff, P., Buckner, J., Zamorano, L., Mehta, M., Curran Jr., W., 2004. Randomized comparison of stereotactic radiosurgery followed by conventional radiotherapy with carmustine to conventional radiotherapy with carmustine for patients with glioblastoma multiforme: Report of Radiation Therapy Oncology Group 93-05 protocol. *International Journal of Radiation Oncology Biology Physics* 60, 853–860. doi:10.1016/j.ijrobp.2004.04.011.

Stockhammer, F., Plotkin, M., Amthauer, H., Landeghem, F., Woiciechowsky, C., 2008. Correlation of F-18-fluoro-ethyl-tyrosin uptake with vascular and cell density in non-contrast-enhancing gliomas. *Journal of Neuro-Oncology* 88, 205–210. doi:10.1007/s11060-008-9551-3.

Stupp, R., Brada, M., van den Bent, M., Tonn, J.C., Pentheroudakis, G., Group, E.G.W., 2014. High-grade glioma: ESMO clinical practice guidelines for diagnosis, treatment and follow-up. *Annals of Oncology* 25, 93–101. doi:10.1093/annonc/mdu050.

Stupp, R., Mason, W., Van Den Bent, M., Weller, M., Fisher, B., Taphoorn, M., Belanger, K., Brandes, A., Marosi, C., Bogdahn, U., Curschmann, J., Janzer, R., Ludwin, S., Gorlia, T., Allgeier, A., Lacombe, D., Cairncross, J., Eisenhauer, E., Mirimanoff, R., 2005. Radiotherapy plus concomitant and adjuvant temozolomide for glioblastoma. *New England Journal of Medicine* 352, 987–996. doi:10.1056/NEJMoa043330.

Subramanian, S., Ghafoori, A., Scheufele, K.M., Himthani, N., Davatzikos, C., Biros, G., 2023. Ensemble Inversion for Brain Tumor Growth Models With Mass Effect. *IEEE Transactions on Medical Imaging* 42, 982–995. doi:10.1109/TMI.2022.3221913.

Subramanian, S., Gholami, A., Biros, G., 2019. Simulation of glioblastoma growth using a 3D multispecies tumor model with mass effect. *Journal of mathematical biology* 79, 941–967. doi:10.1007/s00285-019-01383-y.

Subramanian, S., Scheufele, K., Himthani, N., Biros, G., 2020a. Multitlas Cal-

ibration of Biophysical Brain Tumor Growth Models with Mass Effect. Medical image computing and computer-assisted intervention : MICCAI ... International Conference on Medical Image Computing and Computer-Assisted Intervention 12262, 551–560. doi:10.1007/978-3-030-59713-9_53.

Subramanian, S., Scheufele, K., Mehl, M., Biros, G., 2020b. Where did the tumor start? An inverse solver with sparse localization for tumor growth models. *Inverse Problems. An International Journal on the Theory and Practice of Inverse Problems, Inverse Methods and Computerized Inversion of Data* 36. doi:10.1088/1361-6420/ab649c.

Swanson, K., Alvord E.C., Jr., Murray, J., 2000. A quantitative model for differential motility of gliomas in grey and white matter. *Cell Proliferation* 33, 317–329. doi:10.1046/j.1365-2184.2000.00177.x.

Tripathi, S., Vivas-Buitrago, T., Domingo, R.A., Biase, G.D., Brown, D., Akinduro, O.O., Ramos-Fresnedo, A., Sherman, W., Gupta, V., Middlebrooks, E.H., Sabsevitz, D.S., Porter, A.B., Uhm, J.H., Bendok, B.R., Parney, I., Meyer, F.B., Chaichana, K.L., Swanson, K.R., Quiñones-Hinojosa, A., 2021. IDH-wild-type glioblastoma cell density and infiltration distribution influence on supramarginal resection and its impact on overall survival: A mathematical model. *Journal of Neurosurgery* 136, 1567–1575. doi:10.3171/2021.6.JNS21925.

Tunc, B., Hormuth, D., Biros, G., Yankeelov, T.E., 2021. Modeling of Glioma Growth With Mass Effect by Longitudinal Magnetic Resonance Imaging. *IEEE transactions on bio-medical engineering* 68, 3713–3724. doi:10.1109/TBME.2021.3085523.

Unkelbach, J., Menze, B.H., Konukoglu, E., Dittmann, F., Le, M., Ayache, N., Shih, H.A., 2014. Radiotherapy planning for glioblastoma based on a tumor growth model: Improving target volume delineation. *Physics in Medicine & Biology* 59, 747. doi:10.1088/0031-9155/59/3/747.

van Herten, R.L.M., Chiribiri, A., Breeuwer, M., Veta, M., Scannell, C.M., 2022. Physics-informed neural networks for myocardial perfusion MRI quantification. *Medical Image Analysis* 78, 102399. doi:10.1016/j.media.2022.102399.

Viguerie, A., Grave, M., Barros, G.F., Lorenzo, G., Reali, A., Coutinho, A.L.G.A., 2022. Data-Driven Simulation of Fisher–Kolmogorov Tumor Growth Models Using Dynamic Mode Decomposition. *Journal of Biomechanical Engineering* 144. doi:10.1115/1.4054925.

Wang, S., Sankaran, S., Perdikaris, P., 2022a. Respecting causality is all you need for training physics-informed neural networks. doi:10.48550/arXiv.2203.07404, arXiv:2203.07404.

Wang, S., Teng, Y., Perdikaris, P., 2021. Understanding and Mitigating Gradient Flow Pathologies in Physics-Informed Neural Networks. *SIAM Journal on Scientific Computing* 43, A3055–A3081. doi:10.1137/20M1318043.

Wang, S., Yu, X., Perdikaris, P., 2022b. When and why PINNs fail to train: A neural tangent kernel perspective. *Journal of Computational Physics* 449, 110768. doi:10.1016/j.jcp.2021.110768.

Wu, C., Lorenzo, G., Hormuth, D.A., Lima, E.A.B.F., Slavkova, K.P., DiCarlo, J.C., Virostko, J., Phillips, C.M., Patt, D., Chung, C., Yankeelov, T.E., 2022. Integrating mechanism-based modeling with biomedical imaging to build practical digital twins for clinical oncology. *Biophysics Reviews* 3, 021304. doi:10.1063/5.0086789.

Xu, C., Cao, B.T., Yuan, Y., Meschke, G., 2023. Transfer learning based physics-informed neural networks for solving inverse problems in engineering structures under different loading scenarios. *Computer Methods in Applied Mechanics and Engineering* 405, 115852. doi:10.1016/j.cma.2022.115852.

Yan, H., Romero-López, M., Benítez, L., Di, K., Frieboes, H., Hughes, C., Bota, D., Lowengrub, J., 2017. 3D mathematical modeling of glioblastoma suggests that transdifferentiated vascular endothelial cells mediate resistance to current standard-of-care therapy. *Cancer Research* 77, 4171–4184. doi:10.1158/0008-5472.CAN-16-3094.

Yang, L., Meng, X., Karniadakis, G.E., 2021. B-PINNs: Bayesian physics-informed neural networks for forward and inverse PDE problems with noisy data. *Journal of Computational Physics* 425, 109913. doi:10.1016/j.jcp.2020.109913.

Zheng, H., Huang, Y., Huang, Z., Hao, W., Lin, G., 2023. HomPINNs: Homotopy physics-informed neural networks for solving the inverse problems of nonlinear differential equations with multiple solutions. doi:10.48550/arXiv.2304.02811, arXiv:2304.02811.

Zhu, A., 2022. Accelerating Parameter Inference in Diffusion-Reaction Models of Glioblastoma Using Physics-Informed Neural Networks. *SIAM Undergraduate Research Online* 15. doi:10.1137/22S1472814.